IRAQI JOURNAL OF APPLIED PHYSICS

The *Iraqi Journal of Applied Physics (IJAP)* is a peer reviewed journal of high quality devoted to the publication of original research papers from applied physics and their broad range of applications. IJAP publishes quality original research papers, comprehensive review articles, survey articles, book reviews, dissertation abstracts in physics and its applications in the broadest sense. It is intended that the journal may act as an interdisciplinary forum for Physics and its applications. Innovative applications and material that brings together diverse areas of Physics are particularly welcome. Review articles in selected areas are published from time to time. It aims to disseminate knowledge; provide a learned reference in the field; and establish channels of communication between academic and research experts, policy makers and executives in industry, commerce and investment institutions. IJAP is a quarterly specialized periodical dedicated to publishing original papers, letters and reviews in: Applied & Nonlinear Optics, Applied Mechanics & Thermodynamics, Digital & Optical Communications, Electronic Materials & Devices, Laser Physics & Applications, Plasma Physics & Applications, Quantum Physics & Spectroscopy, Semiconductors & Optoelectronics, Solid State Physics & Applications, Alternative and Renewable Energy, and Computers and Networks.

ISSN (Print): 1813-2065, ISSN (Online): 2309-1673, ISSN (Letters): 1999-656X

EDITORIAL BOARD

Editorial Office:
P. O. Box 55259, Baghdad 12001, IRAQ
Website: www.iraqiphysicsjournal.com
Emails: info@iraqiphysicsjournal.com, editor_ijap@yahoo.co.uk, editor@ijaponline.com

ADVISORY BOARD

SPONSORED AND PUBLISHED BY
THE IRAQI SOCIETY FOR ALTERNATIVE AND RENEWABLE ENERGY SOURCES & TECHNIQUES (I.S.A.R.E.S.T.)

IRAQI JOURNAL OF APPLIED PHYSICS

ISSN (Print): 1813-2065, ISSN (Online): 2309-1673, ISSN (Letters): 1999-656X

" INSTRUCTIONS TO AUTHORS "

CONTRIBUTIONS

Contributions to be published in this journal should be original research works, i.e., those not already published or submitted for publication elsewhere, individual papers or letters to editor.
Manuscripts should be submitted to the editor at the mailing address:
Iraqi Journal of Applied Physics, Editorial Board, P. O. Box 55259, Baghdad 12001, IRAQ
Website: www.iraqiphysicsjournal.com
Email: editor@iraqiphysicsjournal.com, editor_ijap@yahoo.co.uk

MANUSCRIPTS

Two hard copies with soft copy on a compact disc (CD) should be submitted to Editor in the following configuration:

- **One-column** Double-spaced one-side A4 size with 2.5 cm margins of all sides
- Times New Roman font (16pt bold for title, 14pt bold for names, 12pt bold for headings, 12pt regular for text)
- Letters should not exceed 10 pages, papers should not exceed 20 pages and reviews are up to author.
- Manuscripts presented in English only are accepted.
- English abstract not exceed 150 words
- 4 keywords (at least) should be maintained on (PACS preferred)
- Author(s) should express all quantities in SI units
- Equations should be written in equation form (*italic* and symbolic)
- Figures and Tables should be separated from text
- Figures and diagrams can be submitted in colors for assessment and they will be returned to authors after provide printable copies
- Charts should be indicated by the software used for
- Only original or high-resolution scanner photos are accepted
- For electronic submission, articles should be formatted with MS-Word software.

AUTHOR NAMES AND AFFILIATIONS

It is IJAP policy that all those who have participated significantly in the technical aspects of a paper be recognized as co-authors or cited in the acknowledgments. In the case of a paper with more than one author, correspondence concerning the paper will be sent to the first author unless staff is advised otherwise.
Author name should consist of first name, middle initial, last name. The author affiliation should consist of the following, as applicable, in the order noted:
- Company or college (with department name or company division), Postal address, City, state, zip code, Country name, contacting telephone, and e-mail

REFERENCES

The references should be brought at the end of the article, and numbered in the order of their appearance in the paper. The reference list should be cited in accordance with the following examples:
[1] X. Ning and M.R. Lovell, "On the Sliding Friction Characteristics of Unidirectional Continuous FRP Composites", *ASME J. Tribol.*, 124(1) (2002) 5-13.
[2] M. Barnes, "Stresses in Solenoids", *J. Appl. Phys.*, 48(5) (2001) 2000–2008.
[3] J. Jones, "Contact Mechanics", Cambridge University Press (Cambridge, UK) (2000), Ch.6, p.56.
[4] Y. Lee, S.A. Korpela and R. Horne, "Structure of Multi-Cellular Natural Convection in a Tall Vertical Annulus", Proc. 7th International Heat Transfer Conference, U. Grigul et al., eds., Hemisphere (Washington DC), 2 (1982) 221–226.
[5] M. Hashish, "Waterjet Technology Development", High Pressure Technology, PVP-Vol. 406 (2000), 135-140.
[6] D.W. Watson, "Thermodynamic Analysis", ASME Paper No. 97-GT-288 (1997).
[7] C.Y. Tung, "Evaporative Heat Transfer in the Contact Line of a Mixture", Ph.D. thesis, Rensselaer Polytechnic Institute, Troy, NY (1982).

PROOFS

Authors will receive proofs of papers and are requested to return one corrected hard copy with a WORD copy on a compact disc (CD). New materials inserted in the original text without Editor permission may cause rejection of paper.

COPYRIGHT FORM

Author(s) will be asked to transfer copyrights of the article to the Journal soon after acceptance of it. This will ensure the widest possible dissemination of information.

OFFPRINTS

Authors will receive offprints free of charge and any additional reprints can be ordered.

SUBSCRIPTION AND ORDERS

Annual fees (4 issues per year) of subscription are:
50 US$ for individuals inside Iraq; **200** US$ for establishments inside Iraq;
100 US$ for individuals abroad; **300** US$ for establishments abroad.
Fees are reduced by 25% for I.S.A.R.E.S.T. members. Orders of issues can be submitted by contacting the editor-in-chief or editorial office at admin@iraqiphysicsjournal.com, or editor_ijap@yahoo.co.uk to maintain the address of issue delivery and payment way.

IRAQI JOURNAL OF APPLIED PHYSICS
Vol. 16, No. 1, January-March 2020, 3-8

Breakdown and Langmuir Electrical Characteristics of Glow Discharge Plasma in DC Reactive Dual-Magnetron Sputtering System

Tawfiq S. Mahdi
Firas J. Kadhim

Department of Physics, College of Science, University of Baghdad, Baghdad, IRAQ

In this work, the breakdown and Langmuir characteristics of dc glow discharge plasma employing dual-magnetron assembly were studied. The electrical characteristics of this system are optimized to use it for reactive sputtering applications. The plasma was generated by electric discharge of argon gas at pressures ranging from 0.1 to 0.8 mbar. Also, a mixture of argon and oxygen was used to generate plasma since oxygen is used as the reactive gas. First, the Paschen's curves for both cases (argon only and argon/oxygen mixture) were plotted as the variation of breakdown voltage with the product of gas pressure (p) and inter-electrode distance (d) (i.e., p.d). The minima of these curves were ranging in 145-208V for different inter-electrode distances. The minima were also determined for the glow discharge of oxygen only to be ranging in 185-320V. In case of argon/oxygen mixture, the minima were ranging in 100-208V. The resistance of the gaseous medium was determined from the I-V characteristics and the argon showed higher resistance when compared to oxygen and argon/oxygen mixture. The plasma parameters, mainly electron and ion temperatures and densities, were determined from the Langmuir probe measurements for argon only and argon/oxygen mixture. Electron and ion temperatures in argon/oxygen mixture were higher than those in only argon. The densities showed contradictive behaviors as the electron density was lower in argon/oxygen mixture, while the ion density was higher in the same mixture.

Keywords: Discharge plasma; Glow discharge; Plasma sputtering; Langmuir probe
Received: 22 December 2019; **Revised:** 13 February 2020; **Accepted:** 20 February 2020

1. Introduction

Cold plasma technologies have found wide-range of applications in material processing for over 30 years and they are now widely used in the preparation of thin film materials, magnetic media, special glasses, metal coatings, etc. [1-5]. In the last decade, great attention has been devoted to the reactive dc magnetron sputtering technique as it has covered a vast range of industrial applications [6,7]. The most commonly used method of generating and sustaining a low-temperature plasma for technical applications is the application of an electric field to a neutral gas [8,9]. Any volume of a neutral gas is always electrically neutral before applying electric field and the gas at room temperature will contains a few electrons and ions [10]. However, a free electron may be released from a molecule by the interaction of cosmic rays or other radioactive radiation or a random high energy collision with another particle [11,12].

The use of plasma for material deposition is widely used in technological and industrial processes. Sputtering is the most popular method for thin film deposition [13,14]. Noble gases are commonly used to generate the plasma because they are almost chemically inert. Generally, plasma is characterized by external parameters such as direct current (dc) input power, substrate bias, gas pressure and flow rate. However, knowledge of these external parameters does not provide adequate understanding of the sputtering process [15,16]. More insight relating to the film composition and growth rate, for example, is provided by investigating the internal plasma parameters. Many diagnostic techniques, such as Langmuir probe [17] are used to measure the electron plasma density (n_e), the space potential (V_{sp}) and the electron temperature (k_BT_e) in cold low-density plasmas [18].

The Langmuir probes are one of the different electric probe diagnostics that are employed today. In a broader sense, the electric probes measure the local plasma parameters by using stationary or slow-time varying electric (and/or magnetic) fields to emit or to collect charged particles from the plasma [19,20]. These measuring techniques constitute an active field of research and are particularly well suited for low-density cold plasmas, such as low pressure electric discharges, ionosphere and space plasmas [21].

The plasma parameters are deduced from the current (I_p), which, in accordance to the bias voltage $V=V_p-V_{sp}$ is composed of ions, electrons or both

[22]. The attracted charges are collected by through the electric field between the bulk plasma and the metallic surface of the probe. This undetermined spatial potential profile extends in the plasma along distances in the order of few Debye lengths (λ_D) and is denominated plasma sheath [23]. In addition, this local electric field also may be altered according to the magnitude of the current (I_p) collected [24]. Therefore, the charge collection process depends on different characteristic lengths, such as the probe size (r_p) and the thickness (or spatial extension) of the plasma sheath attached to the collecting surface, which related to λ_D [25]. In magnetized plasmas, the Larmor radii of electron (r_e) and ion (r_i) also introduce additional lengths, as well as the mean free path (λ) for collisions between electrons and/or ions and neutral atoms in collisional and weakly ionized plasmas [26,27].

In this work, the breakdown and Langmuir characteristics of dc glow discharge plasma employing close-field unbalanced dual-magnetron assembly are studied. The electrical characteristics of this system are optimized to use it for reactive sputtering applications. The plasma is generated by electric discharge of argon gas at different gas pressures. Also, a mixture of argon and oxygen is used to generate plasma since oxygen is used as the reactive gas.

2. Experimental Part

A homemade dc reactive magnetron plasma sputtering system was designed and constructed for thin film deposition purposes. The details of construction will be briefed as follows. Firstly, we started with the main and most important part in the system, the plasma chamber, which is made as a cylinder of stainless steel with 3 mm thickness and 30 cm height. The top and bottom sides of this chamber are closed with stainless steel flanges. The top flange contains three ports for gas supply, pressure gauge and high-voltage electrode (cathode). The bottom flange has two ports for electrode (anode) and vacuum pump. Both electrodes are made from stainless steel and can be cooled by circulating a cooling fluid through a channel inside the electrode to avoid the heat generated due to electric discharge that may affect the growth process of thin films on the substrates.

The dc power supply consists of a high-voltage transformer (220/6kV), a variac (0-220V_{ac}), a current-limiting resistor (15kΩ), high-voltage diodes (10kV_{dc}), and charging capacitor. The gas mixing unit is made of stainless steel to mix the argon and oxygen gases before pumped into the vacuum chamber throughout a needle valve at flow rate of 0-160 sccm.

The vacuum unit contains of a two-stage Edward rotary pump of 24 m^3/h pumping speed to reach base pressure of about 0.01 mbar. An Edward Pirani gauge was used to measure the pressure inside the chamber.

The plasma parameters in low-pressure discharges can be introduced and determined by Langmuir probe, which is relatively simple and cheap, and acceptably accurate. A homemade Langmuir probe consists of tungsten wire of 0.2 mm in diameter inside a capillary glass tube to protect and isolate the wire from the electrical effects in the surrounding. The tip of the wire is bare (~4mm) and immersed in plasma column for diagnostics.

The fabricated probe was used to measure the electrical characteristics (I-V) of plasma generated by dc discharges of argon, oxygen, and argon-oxygen gas mixtures. The I-V characteristics were measured by varying the probe voltage slowly between -100V and +100V to scan as much as large regions of the plasma column.

3. Results and Discussion

3.1 Paschen's Curve

A plasma column is often generated by applying voltage between the electrodes inside an evacuated chamber containing low-pressure gas. When the applied voltage exceeds a certain value known as "breakdown voltage", the gas discharge is converted from non-sustaining into a self-sustaining type. The charged particles (ions and electrons) are produced by the collisional ionization processes of the neutral atoms (argon atoms). The migration of electrons and ions towards the anode and cathode, respectively, leads to pass current throughout the plasma column and form the glow discharge. Figures (1) and (2) show the variation of breakdown voltage between the electrodes as a function of the product of gas pressure (p) by inter-electrode distance (d), which is known as Paschen's curve.

The voltage is initially decreasing with the product $p.d$ from 460V at $p.d$ of 1 mbar.cm to reach a minimum at a product of 6 mbar.cm. Then, the breakdown voltage slowly increases to reach its highest value of about 240V. Similar behavior was observed as different inter-electrode distances were used. The minimum value of breakdown assigns the breakdown voltage.

The mean free path of electrons in a low pressure gas is longer than that in high-pressure gas, therefore, the probability of the collisions is lower and the ionization process is weaker. Since the probability of secondary electron emission is low, then the number of collisions of electrons with neutral atoms during their migration from the cathode to the anode is relatively few. This is why the voltage is decreasing before the breakdown point.

Beyond the breakdown point, the voltage increases slowly with the increase of gas pressure at constant inter-electrode distance, i.e., the ionization cross section increases with the increase of the $p.d$

product. Therefore, electrons need more kinetic energy to ionize the neutral atoms [28].

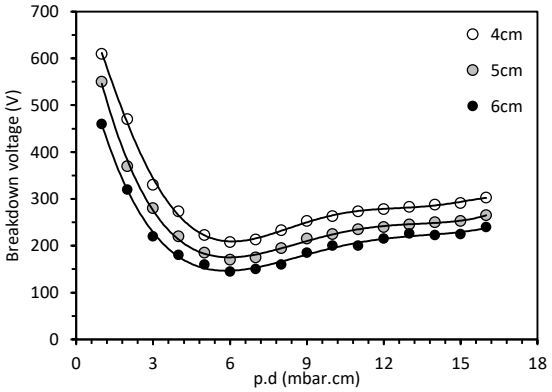

Fig. (1) Paschen's curves for argon gas discharges

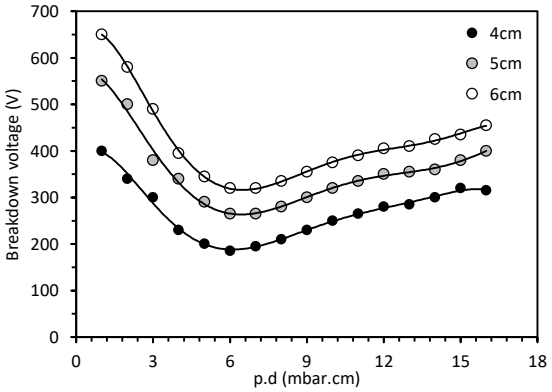

Fig. (2) Paschen's curves for O_2 gas discharges

From these results, it can be noted that the oxygen gas has breakdown voltage greater than that of argon gas as the collisional cross section of the gas depends on its secondary electron coefficient and electronegative. In general, the gases of larger atoms or molecules have larger collisional cross sections [29].

It is well-known in the plasma sputtering systems that two or more gases are used; at least one of them is working gas, such as argon, which is ionized to produce plasma column as well as the ions to hit the target to be sputtered. The other gas (or gases) is the reactive gas, such as oxygen, to react with the sputtered atoms and form the required compound (oxides when oxygen is used). For this reason, the ratio Ar/O_2 in gas mixture is considered as an important parameter in thin film deposition processes. Figure (3) shows the variation of the breakdown voltage as a function of gas pressure at constant inter-electrode distance (4cm) for $Ar:O_2$ mixture with ratio of 1:1 when compared to the same variation for discharge of argon only and oxygen only. The minimum of the $Ar:O_2$ mixture (~185V) is higher than that of argon only (~100V) and lower than that of oxygen only (~208V).

The electrical characteristics of discharge plasma are very significant to introduce the homogeneity of the generated plasma. Different mixing ratios of $Ar:O_2$ were characterized at inter-electrode distance of 4 cm, as shown in Fig. (4), to determine the mixing ratio at which the optimum samples are prepared. Using mixing ratio of 1:1, an increase in the discharge current was observed, which is higher than that observed when only argon is used to generate the plasma, while it is lower than that observed when only oxygen is used to generate plasma. The difference in voltage between the 1:1 mixing ratio (185V) and oxygen only (208V) is relatively small (~23V), which is attributed to the major contribution of oxygen molecules due to the ionization by primary electrons. At discharge voltages higher than 250V, the difference is clearly observed because the secondary electrons are accelerated by higher electric field (*V/d*) and then the ionization rate of oxygen molecules by collisions with these electrons is consequently increased.

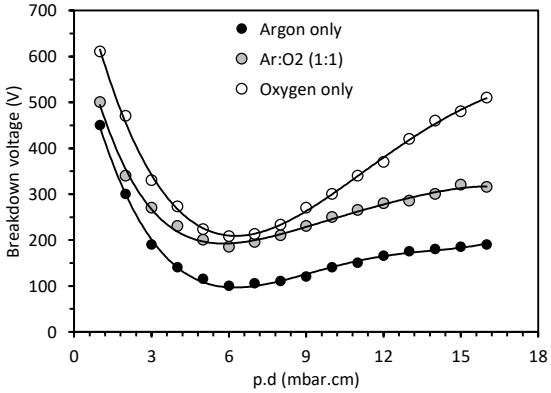

Fig. (3) Paschen's curves for different Ar/O_2 gas mixtures

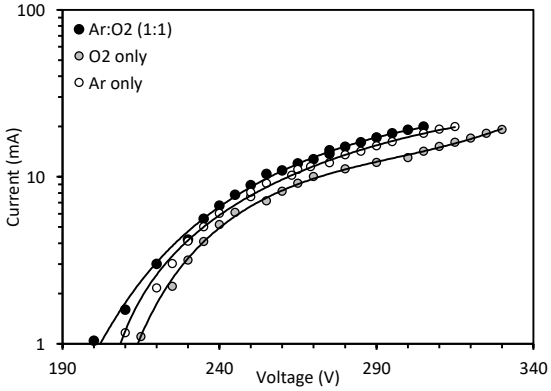

Fig. (4) Discharge current-voltage characteristics for argon only, oxygen only, and argon/oxygen mixture of 1:1 ratio

Figures (5) and (6) show the Langmuir probe current variation with voltage discharge of argon gas and argon-oxygen gas mixture. The homogeneity of plasma column was reasonably affected by the presence of oxygen in the gas mixture as the plasma column has large dimensions when compared to the mean free path of electrons. Also, there is an inverse relationship between the collision probabilities of electrons with their mean free path. The plasma diagnostic was carried out at low pressure (0.1 mbar) and it was found that the mean free path of electrons

is long but definitely shorter than the inter-electrode distance. The electron density, ion density, and the variation of electron temperature as functions of gas pressure were determined as shown in the table (1). Electron temperature (T_e) was obtained by plotting the logarithm of the collected probe current versus probe voltage for the electron retardation region. The slope of the linear behavior of $Ln(I_e)$ versus V curve gives the electron temperature [30].

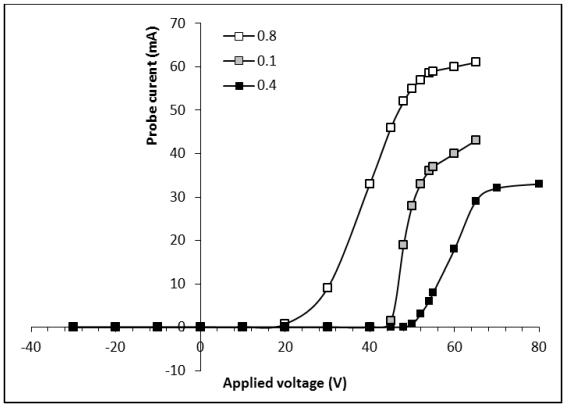

Fig. (5) The I-V characteristics of Langmuir probe for argon discharge plasma at different gas pressures

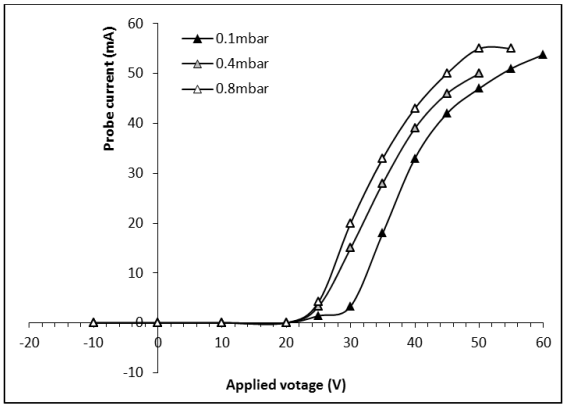

Fig. (6) The I-V characteristics of Langmuir probe for Ar:O_2 discharge plasma at different gas pressures

As indicated in table (1), the electron and ion densities are varied as functions of gas pressure in both cases: argon only and argon/oxygen mixture. Similar behaviors are observed when the Langmuir probe is positioned at the center point of the inter-electrode distance.

Table (1) Parameters of Ar only and Ar:O_2 plasmas at discharge voltage of 3kV

Pressure (mbar)	T_e (eV)	n_e x10^{16} (m^{-3})	T_i (eV)	n_i x10^{16} (m^{-3})
Argon only				
0.1	2.156	2.629	0.523	1.754
0.4	1.956	2.492	0.523	1.842
0.8	1.012	2.203	0.705	1.864
Ar/O_2				
0.1	3.909	1.52	1.568	2.762
0.4	2.507	1.347	1.917	2.861
0.8	1.425	1.301	1.944	2.883

Figure (7) shows the variation of electron and ion temperatures with gas pressure for the argon only and argon/oxygen mixture. It is clear from Fig. (7a) that the electron temperature (T_e) is decreased as the gas pressure is increased for both cases. Electron temperature in the argon/oxygen mixture is higher than that in argon discharge and this is attributed to the decrease in the mean free path as oxygen molecules are added to the argon atoms. At low gas pressures (<0.3 mbar), the difference in electron temperature is larger than that at higher gas pressures, which is also ascribed to the reduction in mean free path with increasing gas pressure.

As shown in Fig. (7b), ion temperatures (T_i) are reasonably lower than electron temperatures for all values of gas pressures. Ion temperature in the argon/oxygen mixture is higher than that in argon discharge due to the reduction in mean free path and hence the ions acquire much more energy by collisions.

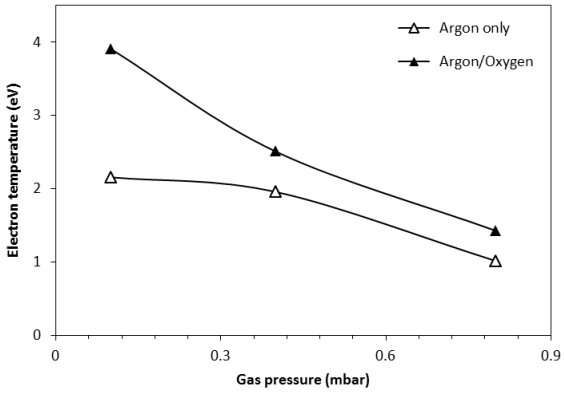

(a)

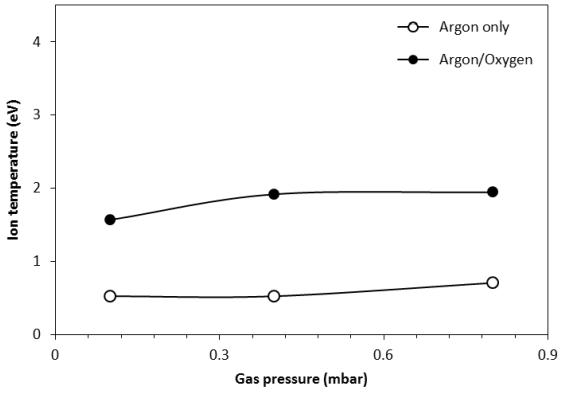

(b)

Fig. (7) Variation of electron and ion temperatures with gas pressure for plasma produced by electric discharge of (a) argon only and (b) argon:oxygen mixture

From both figures, the electron temperatures are four times higher than ion temperatures at argon gas pressure of 0.1 mbar and this difference is decreased with increasing gas pressure. The same behavior is observed in the argon/oxygen mixture but the maximum difference between electron and ion temperatures is about 250%. It is obvious that the ability of electrons to move through the applied

electric field is higher than that of ions due to their lower mass. Accordingly, the decrease in the mean free path results in corresponding increase in collisions between the particles in the discharge volume as they traverse shorter distances before collide with other neutral particles (atoms) and acquire much more energy due to the inelastic collisions [31].

Figure (8) shows the variation of electron and ion densities with gas pressure for the argon only and argon/oxygen mixture. Electron density is reasonably decreased due to the addition of oxygen to the argon in the gas mixture, as shown in Fig. (8a). The difference between the two conditions is slightly reduced at higher gas pressures because the production of more electrons at higher pressures of argon gas is restricted by the fact that the molecular gas species (O_2) cause high energy loss due the excitation of vibrational states [32]. Electrons suffer from collisions with the neutral particles, then they ionizing them. Furthermore, the electronegativity of gas (O_2) decreases the electron density with increasing the oxygen percentage due to the attachment of the electron.

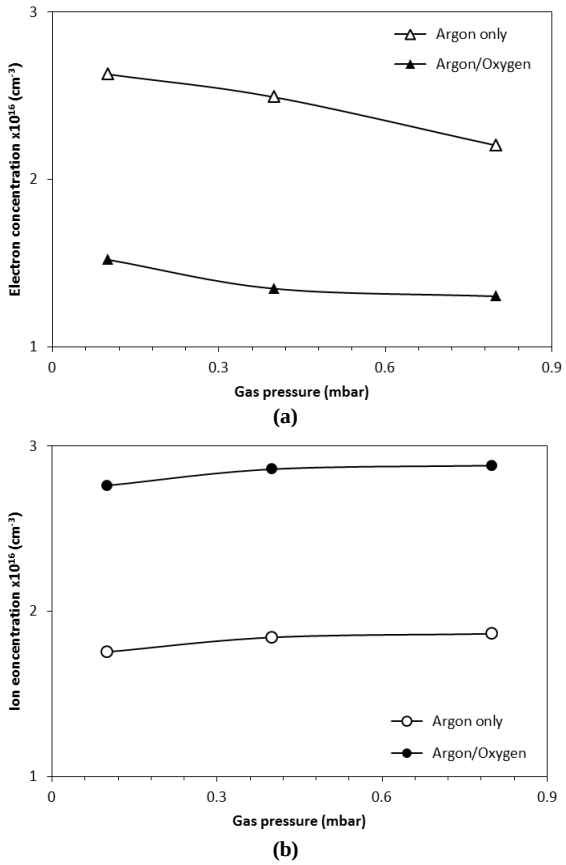

Fig. (8) Variation of electron and ion densities with gas pressure for plasma produced by electric discharge of (a) argon only and (b) argon:oxygen mixture

Contradicting to the behavior of electron density with gas pressure, the ion density is increased in the argon/oxygen gas mixture because the oxygen molecule is separated into two atoms. This results in lower mean free path and hence higher collisional ionization and production of more electrons to be used for sustaining the glow discharge. Consequently, more ions (O^+) are available in the discharge volume and not participating to the current flowing through the plasma column and consuming electrons but not ions [8].

4. Conclusions

According to the results obtained from this work, the homemade dc magnetron plasma sputtering system was characterized to introduce its performance in accordance to electrical characteristics, Paschen's law and governing properties of such deposition systems. The I-V characteristics of gas discharges were determined as plasma system was operated in the abnormal glow discharge region, which is very important parameter for sputtering technique. The Paschen's curves for different gas discharges were determined both experimentally and theoretically and the experimental results were in agreement to those of theoretical treatments with some deviation due to the experimental restrictions included. As well, this system was found to satisfy the requirements of deposition of high-quality thin films from different materials.

References

[1] F.J. Kadhim and A.A. Anber, "Fabrication of Nanostructured Silicon Nitride Films by Reactive DC Magnetron Sputtering for Gas Sensing Applications", *Proc. IMechE, Part N, J. Nanoeng. Nanosys.*, 231(4), 173-178 (2017).

[2] O.A. Hammadi, M.K. Khalaf and F.J. Kadhim, "Silicon Nitride Nanostructures Prepared by Reactive Sputtering Using Closed-Field Unbalanced Dual Magnetrons", *Proc. IMechE, Part L, J. Mater.: Design and Applications*, 231(5), 479-487 (2017).

[3] M.A. Hameed and Z.M. Jabbar, "Optimization of Preparation Conditions to Control Structural Characteristics of Silicon Dioxide Nanostructures Prepared by Magnetron Plasma Sputtering", *Silicon*, 10(4), 1411-1418 (2018).

[4] O.A. Hammadi and N.E. Naji, "Characterization of Polycrystalline Nickel Cobaltite Nanostructures Prepared by DC Plasma Magnetron Co-Sputtering for Gas Sensing Applications", *Photon. Sens.*, 8(1), 43-47 (2018).

[5] O.A. Hammadi, F.J. Al-Maliki and E.A. Al-Oubidy, "Photocatalytic Activity of Nitrogen-Doped Titanium Dioxide Nanostructures Synthesized by DC Reactive Magnetron Sputtering Technique", *Nonl. Opt. Quant. Opt.*, 51(1/2), 67-78 (2019)

[6] R. Barni et al., "Low Temperature Plasma-Based Sterilization: Overview and State-of-the-Art", *Plasma Process Polymer*, 2 (2005) 64.

[7] O.A. Hammadi, M.K. Khalaf, F.J. Kadhim, "Fabrication and Characterization of UV Photodetectors Based on Silicon Nitride Nanostructures Prepared by Magnetron Sputtering", *Proc. IMechE, Part N, J. Nanoeng. Nanosys.*, 230(1) 32-36 (2016).
[8] M. Lieberman, A. Lichtenberg, **"Principle of plasma discharge and Material"**, John-Wiley and Sons (New York, 1994).
[9] H. Conrads and M. Schmidt, "Plasma generation and plasma sources", *Plasma Source Sci. Technol.*, 9 (2000) 441.
[10] O.A. Hammad et al., "Key Mechanisms of Low-Pressure Glow Discharge in Magnetized Plasmas", *Iraqi J. Appl. Phys.*, 12(3) (2016) 3-12.
[11] B. Chapman, **"Glow Discharge Processes"**, John-Wiley & Sons (New York, 1980).
[12] D.A. Glocker, "Influence of the plasma on substrate heating during low-frequency reactive sputtering of AIN", *J. Vac. Sci. Technol.*, A11 (1993) 2989.
[13] J. Kong et al., "The abnormal structure of nanocrystalline titanium films prepared by d.c. sputtering", *Thin Solid Films*, 207 (1999) 51.
[14] O.A. Hammadi, M.K. Khalaf and F.J. Kadhim, "Fabrication of UV Photodetector from Nickel Oxide Nanoparticles Deposited on Silicon Substrate by Closed-Field Unbalanced Dual Magnetron Sputtering Techniques", *Opt. Quantum Electron.*, 47(12), 3805-3813 (2015).
[15] J.A. Thornton, "Magnetron sputtering: basic physics and application to cylindrical magnetrons", *J. Vac. Sci. Technol.*, 15(2) (1978) 171–177.
[16] O.A. Hammadi et al., "Operation Characteristics of a Closed-Field Unbalanced Dual-Magnetrons Plasma Sputtering System", *Bulg. J. Phys.*, 41 (2014) 24-33.
[17] V. Kaeppelin, M. Carrere and J.M. Layet, "Modeling oxide etching in a magnetically enhanced reactive ion plasma using neural networks", *J. Vac. Sci. Technol.*, A20 (2002) 2.
[18] F.F. Chen, "Collisional, magnetic, and nonlinear skin effect in radio-frequency plasmas", *Phys. Plasmas*, 8 (2001) 6.
[19] B.T. Chiad et al., "Langmuir Probe Diagnostics of Low-Pressure Glow Discharge Plasma Using Argon-Nitrogen Mixtures", *Iraqi J. Appl. Phys.*, 12(3) (2016) 17-26.
[20] O.A. Hammadi et al., "Employment of Magnetron to Enhance Langmuir Probe Characteristics of Argon Glow Discharge Plasma in Sputtering System", *Iraqi J. Appl. Phys.*, 12(4) (2016) 19-28.
[21] I.M. Hutchinson, **"Principles of plasma diagnostics",** Cambridge University Press (Cambridge, 1987) Ch. 3.
[22] M.K. Khalaf, O.A. Hammadi and F.J. Kadhim, "Current-Voltage Characteristics of DC Plasma Discharges Employed in Sputtering Techniques", *Iraqi J. Appl. Phys.*, 12(3) (2016) 11-16.
[23] A.A. Solov'ev et al., "Investigation of Plasma Characteristics in an Unbalanced Magnetron Sputtering System", *Plasma Phys. Rep.*, 35(5) (2009) 399–408.
[24] N. Hershkowitz, O. Auciello and D.L. Flamm, **"How Langmuir probes work. in Plasma Diagnostics. Discharge parameters and chemistry"**, Vol. 1, Academic Press (Boston, 1989), Ch. 3.
[25] B.T. Chiad et al., "Characteristics and Operation Conditions of a Closed-Field Unbalanced Dual Magnetrons Plasma Sputtering System", *Open Access Library J.* (OALib), 1 (2014) e650. DOI:10.4236/oalib.1100650
[26] F.F. Chen, **"Introduction to Plasma Physics and Controlled Fusion",** 2nd ed., Plenum Press (New York, 1984).
[27] Y.P. Raizer, "**Gas Discharge Physics**", Springer-Verlag (Berlin, 1991), Ch. 6 and 8.
[28] L. Yu et al., "Direct-current glow discharges in atmospheric pressure air plasmas", *J. Appl. Phys.*, 91 (2002) 2678-86.
[29] M.K. Khalaf, **"Low-pressure plasma Reactor for Materials Surfaces Processing"**, Ph.D. thesis, University of Baghdad, Iraq (2010).
[30] S.K. Jong and H.K Gon, "Characterization of an Oxygen Plasma By Using a Langmuir Probe in an Inductively Coupled Plasma", *J. Korean Phys. Soc.*, 38 (2001) 3259.
[31] D. Akbar and S. Bilicmen, "Non-uniform axial electric field in argon glow discharge plasma", *Chin. Phys. Lett.*, 23(5) (2006) 1234.
[32] O.A. Hammadi et al., "Magnetic Field Distribution of Closed-Field Unbalanced Dual Magnetrons Employed in Plasma Sputtering Systems", *Iraqi J. Appl. Phys.*, 12(3) (2016) 34-42.

IRAQI JOURNAL OF APPLIED PHYSICS
Vol. 16, No. 1, January-March 2020, 9-14

Enhancement of Current Gain at High Collector Current Densities for Silicon-Germanium Heterojunction Bipolar Transistors

Gagan Khanduri
Brishbhan Panwar

Centre for Applied Research in Electronics
Indian Institute of Technology Delhi
Hauz-Khas, New-Delhi-110016
INDIA

In this work, an NPN Si/SiGe/SiGe graded heterojunction bipolar transistor has been compared with contemporary NPN Si/SiGe/Si double heterojunction bipolar transistor for current gain performance at high collector current densities, using a 2-dimensional device simulator. The analysis predicts that the base-collector homojunction of the first transistor device structure is responsible for improved current gain at high collector current density in comparison with the conventional transistor device and provides the option of operation at higher collector current densities.

Keywords: SiGe DHBT; SiGe GHBT; Current gain; Linear tapering
Received: 6 January 2019; **Accepted:** 25 Febrary 2020

1. Introduction

A bipolar junction transistor (BJT) can be represented by a two-diode n-p-n or p-n-p structure s shown in Fig. (1), which also defines the symbols and the three terminals of the devices (emitter, base and collector) plus the terminal voltages and currents.

The arrow on the emitter lead serves two purposes. First, it distinguishes between the collector and emitter terminals which normally cannot be interchanged. Second, the arrow denotes the direction of conventional current flow through the device, providing discrimination between the symbol for the n-p-n transistor and its p-n-p counterpart.

In normal operation, the emitter-base junction is forward biased and the collector-base junction reverse biased. For the schematic n-p-n structure of Fig. (2a), electrons are injected from the n-type emitter into the base and, at the same time, holes are injected from base to emitter. To improve device efficiency, the doping level of the base region is made much lower than that of the emitter; essentially only electron current flows across the emitter-base junction with the injection level controlled (exponentially) by the base-emitter forward bias potential (V_{BE}), as

$$I_E \propto exp\left(\frac{qV_{BE}}{KT}\right) \quad (1)$$

Electrons injected from the emitter become minority carriers in the p-type base and, since the collector-base junction is reverse biased, these minority carriers which cross the base by diffusion are swept across the collector-base transition region.

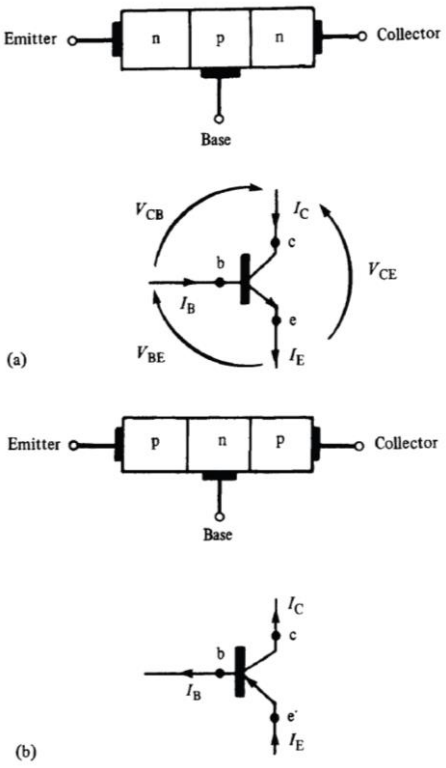

Fig. (1) Schematic structures, symbols, voltages and currents for (a) n-p-n and (b) p-n-p BJTs

Because the electrons spend a finite time in transit through the base region, some recombine with holes; the holes involved in this recombination are replaced by positive charge flow into the base (via its

connection to the bias source) resulting in a base current (I_B).

Operation of the transistor may be summarized by reference to Fig. (2b). The electron current at the collector is almost all of the current injected from the emitter diminished only by that lost as base current due to recombination. This consideration neglects hole injection from base to emitter and hole leakage from collector to base, both of which contribute to device current and hence degrade total efficiency.

The term bipolar is applied to junction transistors of the type described above since two types of charge carrier (holes and electrons) are involved in the operation of the device. Unipolar, or field-effect, transistors rely on only one type of carrier.

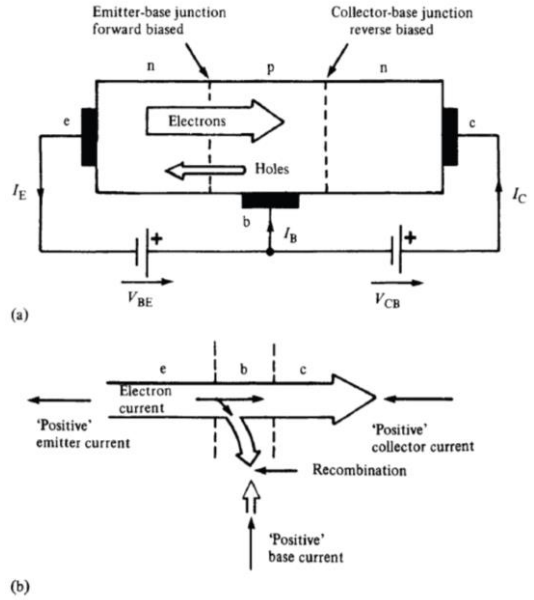

Fig. (2) (a) Schematic structures n-p-n BJTs, and (b) current notation of BJT operation

Silicon-Germanium technology provides the option of band gap engineering along with the compatibility with the present day silicon process technology and hence provides the option of integrating the SiGe technology for advancement of present day device field. Extremely high cut-off frequency of 30 GHz and maximum frequency of oscillation of 50 GHz in the Si/SiGe/Si NPN double heterojunction bipolar transistors (DHBTs) had already been reported for use in mobile communication applications [1]. One important aspect of operation of SiGe devices is their requirement of operation at high current densities to achieve high cut-off frequency performance. Moreover, the scaling down of present day electronic devices forces the operation of these devices at very high collector current densities ($> 10^5$ A/cm^2). Therefore, the operation and performance of SiGe heterostructure transistors at high collector current densities is of prime concern for the microelectronics researchers and process engineers.

It has been already reported that the NPN Si/SiGe/Si DHBT structures exhibit rapid fall in the current gain at high collector current densities [2]. This rapid fall in the current gain leads to the fall in transistor efficiency and make it impractical for use at high collector current densities. The degraded current gain at high collector current densities in DHBT structures is attributed to the formation of retarding potential barrier for electrons at base-collector junction. The velocity saturation of electrons in collector and the valence band offset for holes at base-collector junction leads to the formation of retarding potential barrier. The analysis of NPN Si/SiGe/Si DHBT structure by Cottrel and Yu [2] shows the drop in the collector current density curve as the forward base-emitter bias exceeds approximately 0.77V, predicting a sharp falloff in current gain of the transistor above 0.77V. Therefore, some alternate HBT structures without valence band offset for holes at base-collector junction need to be evolved for improving the transistor current gain and efficiency at high collector currents.

In the present work, the conventional NPN SiGe DHBT structure with uniform 20 at% of germanium in base is simulated to supplement the earlier reported results on the formation of retarding potential barrier. These results are used as the basis for comparing the structures evolved to improve the current gain at high current densities. The objective has been to transform the base-collector heterojunction with the closest approximation to homojunction. Therefore, in the present work the GHBT structure with a uniform Ge at% in base region and a linearly graded germanium at% in collector has been chosen with a perfect homojunction at base-collector metallurgical junction. The base-collector homojunction completely inhibits the formation of retarding potential barrier due to valence band offset and the grading of germanium ensures the strained behavior and stability of the SiGe layers [3]. A further advantage of choosing the NPN GHBT structure lies in the fact that the process of growing a box-type uniform SiGe base layer over a linearly graded SiGe collector region is more practical to achieve dislocation free strained base and collector SiGe layers.

A two-dimensional MEDICI device simulator, known for its authenticated results at the device level for SiGe HBT structures [4], has been used in the present analysis and the high doping and electric field models have been included. The performance of both the HBT structures for current gain is compared and authenticated by investigating the conduction band electron energy, net carrier concentration profiles, metallurgical junction, and dependence of collector current density on base-emitter bias voltage. A theoretical formulation has been provided to supplement the improved performance obtained in the proposed Si/SiGe/SiGe heterostructure in comparison with SiGe DHBT structure.

2. Theory

In NPN silicon BJT the finite electron concentration n_c in collector-base space charge layer is necessary to sustain the flow of collector current in the transistor. An expression relating the electron density n_c with the collector current density J_c for the constant drift velocity v_{dsat} condition is given as [5]:

$$J_c = qv_{dsat}n_c \quad (2)$$

At sufficiently high collector current density the high electron concentration in the space charge region of collector lowers the potential barrier at base-collector junction. This leads to the onset of Kirk phenomenon [5] where the base-collector junction shifts into the collector space-charge region resulting in the vertical widening of the effective neutral base region width. The total voltage across base-collector junction (V_{bctot}) is the sum of built in potential barrier at base-collector junction (V_{bi}) and the terminal base-collector voltage (V_{bct}). At the onset of Kirk phenomenon, (at Kirk current density J_k), the electron density in base-collector space charge region, n_c (= n_k, electron density at start of Kirk effect), is related with the device parameters and V_{bctot} by the expression:

$$n_c = N_c + \left\{\left((2\varepsilon)\frac{V_{bctot}}{qW_c^2}\right)\right\} \quad (3)$$

where N_c is the collector-doping concentration, ε is the dielectric constant for Si, q is the electronic charge and W_c is the collector width as now whole collector width corresponds to space charge region

In Si BJT, at the onset of Kirk phenomenon, holes are injected into the collector from the base to compensate the electron charge in collector, resulting in the formation of the current induced base. However, for SiGe DHBTs having a sizable alloy mole fraction, there is a valence band discontinuity for holes at base-collector junction. This valence band discontinuity suppresses the hole injection into the collector as n_c exceeds n_k. Eventually, there will be an accumulation of mobile electrons in collector due to velocity saturation and an accumulation of holes in base due to valence band offset at base-collector junction. The combination of these mobile electrons together with localized holes form a dipole layer and in turn give rise to an electric field E_0. A further increase in the collector current density will consequently increase the dipole strength and increases the electric field E_0. The presence of the electric field E_0 at base-collector heterojunction gives rise to a retarding potential barrier (V_{bp}) in conduction band, which would oppose the electrons flowing from emitter to collector through base. An increased electron density in the base at base-collector junction $n_{(Wb)}$ is now required to support and maintain the electron density n_c and collector current density J_c. The electron density n_c in base-collector space charge region for collector density J_c, in SiGe DHBT derived from the basic Poisson's equation is:

$$n_c = N_c + \left\{\left((2\varepsilon)\frac{V_{bctot} + E_0W_c}{qW_c^2}\right)\right\} \quad (4)$$

The electron density in base at base-collector junction $n_{(Wb)}$ required to maintain the n_c inside base-collector space charge region is simply given by using current continuity and Boltzmann statistics across the retarding potential barrier V_{bp}:

$$n_{(Wb)} = n_c \exp\left(\frac{qV_{bp}}{KT}\right) \quad (5)$$

where $KT/q = V_T$ is the thermal voltage

The retarding potential barrier V_{bp} for electrons can be expressed as:

$$V_{bp} = \Delta E_v + KT\ln\left[\frac{J_c}{qv_{dsat}N_b} - \frac{N_c}{N_b} - \frac{2\varepsilon(V_{bctot})}{qN_bW_c^2}\right] \quad (6)$$

where ΔE_v is the valence band discontinuity for holes and N_b is the neutral base width. Solving Eq. (4), (5) and (6) for a uniformly doped base gives the effect of bias dependent retarding potential barrier V_{bp} and base-emitter biasing V_{be} on the collector current density J_c as:

$$J_c = \left[\left(\frac{qD_nn_{io}^2}{W_bN_b}\right)\left(\frac{e^{\left(\left(qV_{be}+\Delta E_v-V_{bp}\right)/KT\right)}}{1+\frac{D_ne^{\left(V_{bp}/KT\right)}}{W_bv_{dsat}}}\right)\right] \quad (7)$$

where, n_{i0} is the intrinsic carrier concentration. The modified value of electron density in base at emitter-base junction $n_{(0)}$ in term of V_{bp} is expressed as:

$$n_{(0)} = \left[\left(n_c\left(v_{dsat}W_b\right)\right) + \left(n_c\exp\left(\frac{qV_{bp}}{KT}\right)\right)\right] \quad (8)$$

where $[n_c(v_{dsat}\,W_b)/D_{nb}]$ is the electron density in the base at the base-emitter junction corresponding to the electron density in base-collector space-charge region n_c. The second term in Eq. (8), $[n_c\{\exp(qV_{bp}/KT)\}]$ is the electron density in base at the base-emitter junction as a result of increased electron concentration in base at base-collector junction because of the retarding potential barrier at base-collector junction.

The relation of the effective band offset δE_v and valence band discontinuity ΔE_v with $n_{(0)}$ and V_{be} (for a specific J_c) is expressed as:

$$V_{be} = \left[\begin{array}{l} V_t \ln\left\{ \left(\frac{n_{(0)}^2}{n_{i0}^2} \right) + \left(\frac{n_{(0)} N_b}{n_{i0}^2} \right) \right\} \\ - \frac{\delta(E_v)}{q} \end{array} \right] \quad (9)$$

The substitution of the expression for $n_{(0)}$ from the Eq. (8) in Eq. (9) predicts the necessity for an increase in V_{be} to account for the increase in $n_{(0)}$ required to sustain the collector current density J_c. This requirement of increase in V_{be} for a given collector current density J_c will be reflected as a fall in the current gain of the DHBT structure. This prediction is consistent with the discussion of Eq. (7) where an increase in retarding potential barrier V_{bp} at high collector current density predicts a fall in the DHBT collector current density J_c and current gain.

The analysis of SiGe DHBT illustrates the formation of retarding potential barrier at base-collector junction due to valence band offset for holes. The theory also predicts a fall in the current gain at high collector current density as a consequence of this retarding potential V_{bp}. Whereas, the proposed GHBT structure with uniform Ge profile in base and grading of Ge at% in collector avoids the retarding potential barrier for electrons at base collector homojunction. Consequently, this structure promises an improved current gain at high collector current density in comparison with SiGe DHBT structure.

3. Simulation Results for SiGe DHBT and GHBT Structures

The current gain performance of the NPN Si/SiGe/Si DHBT and proposed NPN Si/SiGe/SiGe heterostructure is compared for identical device dimensions, doping densities and bias conditions. The surface emitter doping of 5×10^{19} cm^{-3} and its thickness W_{e1} of 0.2 μm is chosen to provide ohmic contact. The emitter doping of 1×10^{19} cm^{-3} and its thickness W_{e2} of 0.1 μm is selected to lower the emitter-base. The base thickness W_b of 0.05 μm with a uniform base doping of 8×10^{18} cm^{-3} is chosen in both the structures. The collector doping of 10^{17} cm^{-3} and thickness W_c of 0.45 μm have been chosen in both the structures.

The germanium profile in different regions of Si/SiGe/Si DHBT and Si/SiGe/SiGe HBT structures is shown in Fig. (3). An optimized mole fraction of germanium has been chosen to retain the strained behavior and stability of SiGe regions [3]. A uniform 20 at% Ge has been chosen in the base of conventional Si/SiGe/Si Double HBT (DHBT) structure, whereas its collector does not contain any germanium mole fraction. The base-collector homojunction, in the proposed Si/SiGe/SiGe *Graded* HBT (GHBT) structure has been ensured by choosing a uniform 20 at% Ge in base and tapering it linearly to zero at% Ge at the collector ohmic contact.

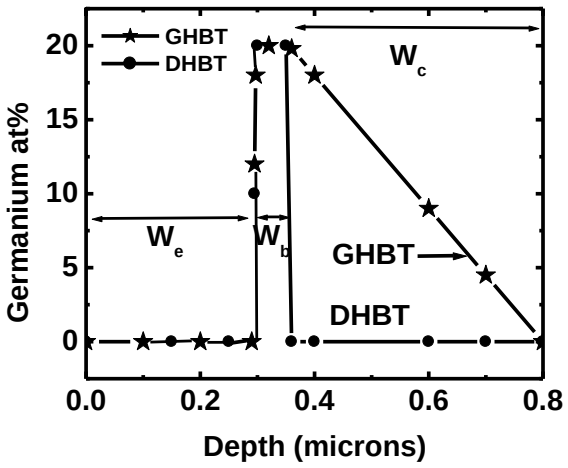

Fig. (3) Ge profile in the emitter, base and collector for the SiGe DHBT and GHBT. W_e, W_b, and W_c are the total emitter, base, and collector width, respectively in the HBTs

The chosen operating conditions of SiGe DHBT and GHBT structure ensures the performance evaluation in the high collector current density region (>10^5 A/cm^2). The simulation results on conduction band electron energy for both the structures include the influence of valence band offset for holes and bandgap narrowing due to the heavily doped base. The electron energy profile shown in Fig. (4), for the collector current density of 9.22×10^5 A/cm^2, predict the total retarding potential barrier V_{bp} of approx. 0.09eV for the conduction band electrons at the base-collector heterojunction in the SiGe DHBT structure. The valence band offset for holes at base-collector heterojunction is observed to contribute 0.06 eV in the total retarding potential barrier in the DHBT structure. This is obtained by excluding the influence of heavy doping effect on band gap narrowing in the base. The simulated result is consistent with the retarding potential barrier of approximately 0.058 eV obtained by solving Eq. (6) for SiGe DHBT accounting only for the valence band offset for holes. Whereas, the formation of such a retarding potential barrier (due to valence band offset for holes) is prohibited by the base-collector homojunction in the GHBT structure. Therefore the simulation results shown in Fig. (4), for the collector current density of 1.6×10^6 A/cm^2 in the GHBT structure, exhibits a small potential barrier of 0.03 eV, which is solely attributed to the high doping in the base. The retarding potential barrier of 0.06 eV in the DHBT structure leads to accumulation of mobile electrons at base-collector heterojunction.

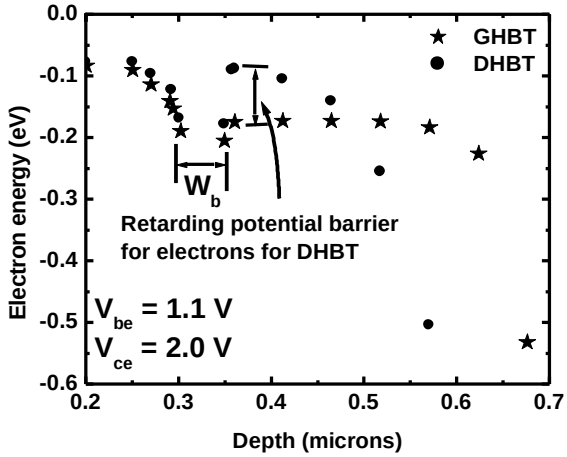

Fig. (4) Conduction band electron energy E_C for SiGe DHBT and GHBT including the effect of valence band offset and band gap narrowing. W_b is the base width

The variation of net carrier concentration with the vertical depth of the SiGe DHBT and SiGe GHBT structures for the chosen bias conditions is shown in Fig. (5). A net carrier concentration of 8.11×10^{19} and 3.93×10^{19} cm^{-3} is obtained in the base of DHBT structure at emitter-base and base-collector junctions, respectively. This corresponds to an electron concentration of 4.36×10^{19} cm^{-3} and 2.92×10^{19} cm^{-3} in the base of DHBT structure at the corresponding metallurgical junctions. Whereas, a lower net carrier concentration of 6.34×10^{18} cm^{-3}, which corresponds to an electron concentration of 1.86×10^{19} cm^{-3}, is obtained, for a higher collector current density of 1.6×10^{6} A/cm^2 at base-collector junction in the base of GHBT structure. The simulation results predict an electron concentration of 3.07×10^{19} cm^{-3} at the emitter-base junction in GHBT structure.

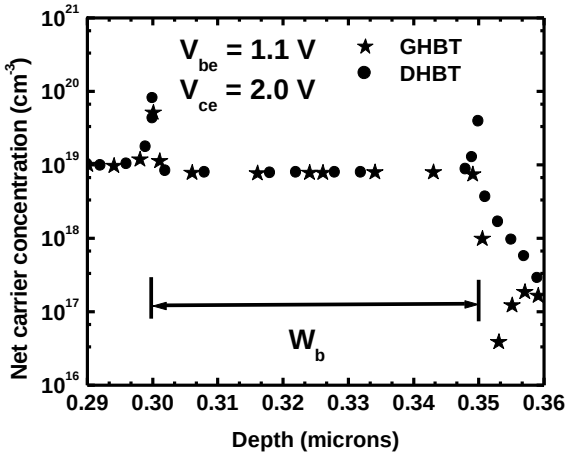

Fig. (5) Net carrier concentration in SiGe DHBT and GHBT at collector-emitter voltage V_{ce} of 2 V and base-emitter voltage V_{be} of 1.1 V. W_b is the base width

This increase in electron concentration at both the metallurgical junctions in the base of DHBT forces the requirement of an associated increase in base-emitter biasing voltage V_{be}.

The dependence of collector current density J_c on the base-emitter bias voltage V_{be}, for the DHBT and GHBT structures, is shown in Fig. (6). The results predict the requirement of base-emitter bias voltage of 1.1 V for the DHBT and 0.97 V for the GHBT structure to sustain the collector current density of 9.22×10^5 A/cm^2. The base-emitter bias voltage for the GHBT structure is observed to increase linearly with the collector current density. Whereas, the collector current density for the DHBT structure approximately saturates above the base-emitter bias voltage of 0.98V. Therefore, at higher collector current densities the DHBT structure needs higher base-emitter bias voltage in comparison with GHBT structure, for sustaining the same collector current density, which will adversely influence the current gain of DHBT in comparison with GHBT structure.

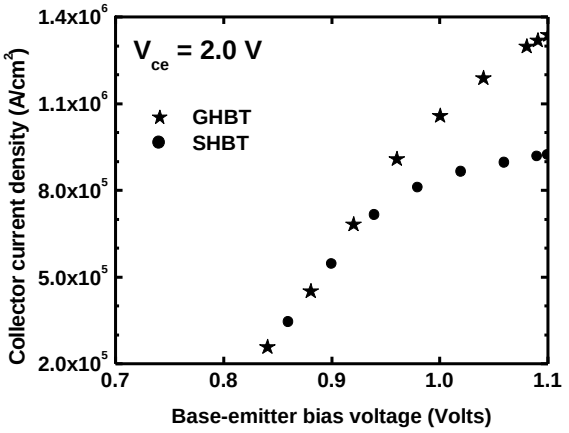

Fig. (6) Dependence of collector current density J_c on base-emitter bias voltage V_{be}

The dependence of current gain on the collector current density for the DHBT and the GHBT structure is shown in Fig. (7). The monotonically decaying behavior of current gain in both the structures for the collector current densities less than 4.0×10^5 A/cm^2 is attributed to the Kirk effect [5] and high-level injection of minority carriers in the base. At higher collector current densities ($>4.0\times10^5 A/cm^2$), the current gain in the GHBT structure falls to 72% of its initial value for twofold change in the current density. Whereas, the current gain in the DHBT structure falls to 10% for twofold change in the collector current density. Therefore, the DHBT shows a sharp fall-off in the current gain in comparison with GHBT structure as the collector current density increases. The results are consistent with fall in the current gain in DHBT structure, predicted by Eq. (7), due to the formation of retarding potential barrier at base-collector junction in the DHBT structure. The results establish superior current gain performance of the GHBT structure in comparison with the DHBT device. Although the results presented in the present work are for the pre-selected doping profiles and

physical parameters of the device but the phenomena of better performance of the GHBT structure over contemporary DHBT structures will be consistent with other device configurations and doping profiles.

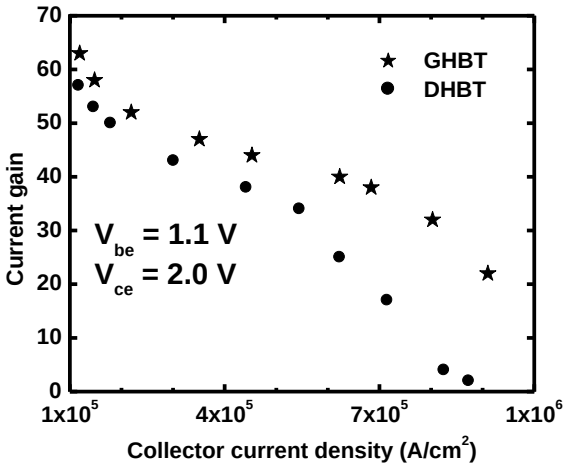

Fig. (7) Current gain versus collector current density plot for NPN SiGe DHBT and GHBT

4. Conclusions

An NPN SiGe GHBT structure with uniform 20 at% germanium in the base and tapering it linearly to zero at% Ge at the collector ohmic contact is proposed to improve the current gain performance of the SiGe HBTs at high collector current densities. The base-collector homojunction inhibits the formation of retarding potential barrier due to absence of valence band offset for holes at base-collector metallurgical junction and 20 at% of germanium and its tapering ensures the strained behavior and stability of the SiGe layers. The absence of retarding potential barrier in SiGe GHBT is observed to provide better current gain performance at high collector current densities in comparison with DHBT structure. A theoretical model for SiGe DHBT has been developed to supplement the simulation results for current gain dependence on the physical parameters and device structure. A comparison of conduction band electron energy, net carrier concentration profile and dependence of collector current density on the base emitter voltage has been provided for the SiGe HBT structures. The theoretical formulation and the simulated results on the current gain performance establish the superiority of the GHBT structure in comparison with the DHBT device configuration at high collector current densities.

References

[1] Andreas Schuppen, "SiGe-HBTs for mobile communication," *Solid State Electronics*, **43**, 1373-1381 (1999).

[2] Zhiping Yu, Peter E. Cottrell and R. W. Dutton,"Modeling and simulation of high-level injection behavior in double heterojunction bipolar transistors," *IEEE Bipolar Circuits and Technology Meeting*, **8.5**, 192-194 (1990).

[3] R. People and J.C. Bean, "Calculation of critical layer thickness versus lattice mismatch for Ge_xSi_{1-x}/Si strained-layer heterostructure" *Applied Physics Letters*, **47** (3), 322-324 (1985).

[4] Md. R Hashim, R. F Lever, and P. Ashburn, "2D simulation of the effects of transient enhanced boron out-diffusion from base of SiGe HBT due to an extrinsic base implant," Solid State Electronics, **43**, 131-140 (1999).

[5] D. J. Roulston, *Bipolar Semiconductor Devices*. McGraw-Hill, New York (1990).

IRAQI JOURNAL OF APPLIED PHYSICS
Vol. 16, No. 1, January-March 2020, 15-20

Oday A. Hammadi

Department of Physics, College of Education, Al-Iraqia University, Baghdad, IRAQ

Analysis of Secondary Electron Emission in Gas Glow Discharges Used for Thin Film Deposition Processes

In this study, the emission coefficient of secondary electrons for some common gas discharges employed in thin film deposition processes and techniques was determined as function of some affecting parameters. This coefficient may play negative role in the optimization of discharge plasma employed for practical uses and applications. Therefore, this coefficient is often minimized even though the experimental conditions are shifted from their optima in order to ensure that the consumption of supplied power is high as much as possible. This study was supported by experimental data from a reactive plasma sputtering system used for deposition of some metal oxide and nitride thin films.

Keywords: Gas discharge; Discharge plasma; Electron emission; Emission coefficient
Received: 14 December 2019; **Revised:** 3 February 2020; **Accepted:** 10 February 2020

1. Introduction

Today, plasma can be generated, controlled and employed in physics laboratories at reasonably low requirement, cost and risk conditions. Over 150 years ago, sputtering was observed for the first time by Grove when he was working on discharge plasma [1,2]. It was really interesting to control a process in which an atom is removed from a target, carried through plasma and deposited on a substrate [3 6]. When plasma is totally and precisely controlled, then the whole sputtering process is accordingly controlled [7 10].

The dc glow discharge has been historically important, both in applications of weakly ionized plasmas and in studying the properties of the plasma medium [11,12]. A dc discharge has one obvious feature, its macroscopic time independence, that is simpler than radiofrequency (rf) discharges. However, the need for the current, which provides the power for the discharge, to be continuous through the dc sheath provides an additional complication to the operation [13-15].

Glow discharge is low-temperature neutral plasma where the number of electrons is equal to the number of ions despite that local but negligible imbalances may exist at walls [7]. Glow discharge is described as self-sustaining plasma, i.e., the avalanche effect of electrons keeps the continuous production of ion species [16,17]. The avalanche condition from the initial applied voltage in a typical low-pressure discharge is shown in Fig. (1) [16].

If an initial voltage is applied on a gas sample between two electrodes at sufficient separation, little current will flow through this sample due to the ionization effects in the gas [18]. As the applied voltage is increased to reach the breakdown voltage, the energy given to ions is increased too that increases their collisions with atoms and electrodes. Accordingly, more ions and electrons are produced due to the ionization and secondary electron emission effects, which lead to increase the flowing current gradually approaching the breakdown point beyond which the avalanche occurs and the current increases drastically in the Townsend discharge region [19].

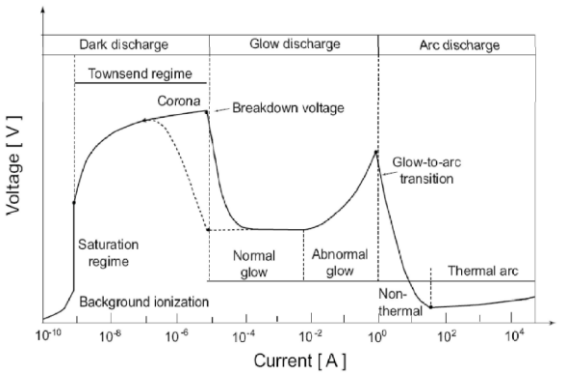

Fig. (1) Different regions of plasma discharge on the I-V characteristics [16]

If an energetic ion approaches the surface of a solid (target), one or all of the following phenomena may occur:

• The ion may be reflected, being getting neutralized in the process.
• The collision of the ion may cause the target to eject an electron, called the secondary electron.
• The ion may become buried in the target.
• The ion collision might be responsible for some structural changes in the target material.
• The ion collision may set up a series of collisions between atoms of the target, leading to the ejection

of one of the target atoms. This ejection process is known as sputtering [20].

Figure (2) summarizes all the phenomena mentioned above. The principles of sputtering can be understood using a simple momentum transfer model, which enables to visualize how atoms are ejected from a surface as a result of two collisions.

The series of collisions in the target, generated by the primary collision at the surface, is known as a collision cascade. It is a matter of probability whether this cascade leads to the sputter ejection of an atom from the surface (which will require at least two collisions) or the cascade heads off into the interior of the target, gradually dissipating the energy of the primary impact, ultimately to lattice vibration. Sputtering ejection is rather energy inefficient, with typically 1% of the incident energy reappearing as the energy of the sputtered atom. The rest of the energy is lost in the form of heating of the chamber walls, parts inside the chamber and the target [21].

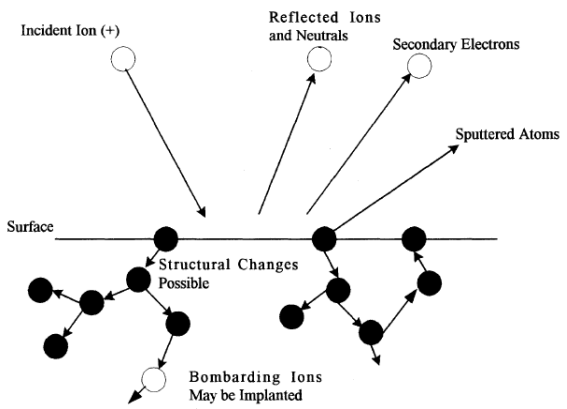

Fig. (2) Interaction of ions with surfaces [21]

Sputtering is complex process, which is highly dependent on number of process parameters, such as deposition pressure, discharge voltage, discharge current, target-to-substrate distance, gas compositions, process gas flow rate, reactive gas flow rate in case of reactive sputtering, substrate biasing, etc. [22-24].

The sputtering process is quantitatively described by the sputtering yield, which is defined as the number of target atoms ejected per incident particle. This yield depends on the target materials and their crystalline structure, the energy of incident particles, and the incidence angle of the bombarding particles [3,25]. When the mass of the bombarding particle is comparable or larger than that of the target atoms, the sputtering yield tends to be greatest. It is relatively independent of the target temperature and whether or not the bombarding species is ionized [25].

In the case where no bias is applied to the collection cylinder, both target and collection cylinder are at the same potential, the calculation of g is straight forward. The electrons are emitted in a cosine distribution with respect to the surface normal and the fraction of electrons that escape through the hole for the ion beam, d_{esc}, is easily calculated. From this, g=l/(l-d_{esc}) can be determined [26]. With a bias on the collection cylinder, two questions must be answered: will electrons that used to escape now be collected? and will electrons that were collected now escape?

In order to answer those questions, the trajectories of emitted electrons was calculated. It was assumed that a constant electric field parallel to the target E_y was maintained (Fig. 3). The approximation of two parallel plates for the collection cylinder and target was found to be good by comparing this situation with the true set up of a flat target and a curved collection plate. The radius of curvature is large compared to the distance between the target and collection cylinder. Thus, the curvature is insignificant.

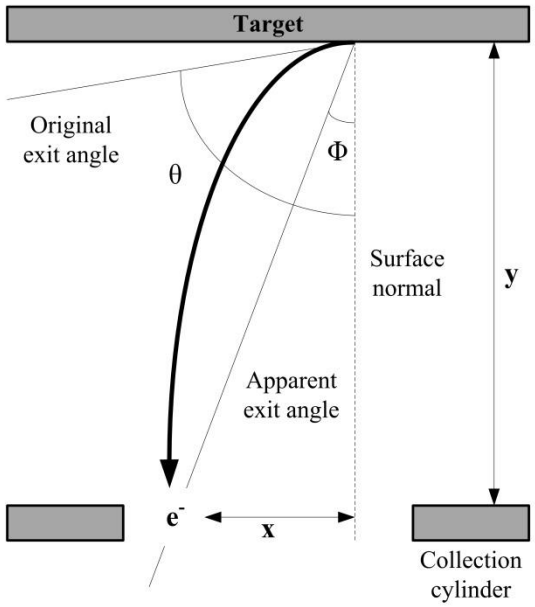

Fig. (3) Explanation of original and apparent exit paths of electron under the effect of electric field in discharge system

2. Modeling and Mathematical Treatment

The breakdown voltage is directly related to the pressure of the gas sample and the mean free path of secondary electrons. This relation between breakdown voltage (V_B) and gas pressure (p) is known as "Paschen's law" and given by [27]:

$$V_B = \frac{pdB}{log(pdA) - log\left(log\left(1+\frac{1}{\gamma_e}\right)\right)} \quad (1)$$

where A and B are constants and their values are determined by the properties of the used gas, as shown in Table (1), d is the inter-electrode distance (i.e., the distance between discharge electrodes), and γ_e is the emission coefficient of the secondary electrons

The breakdown voltage (V_B) depends on the product ($p.d$), and weakly depends on the cathode material that defines the emission coefficient of secondary electrons [13]. As well, the breakdown voltage is proportional to the product $p.d$ at large values of this product and the electric field ($E=V/d$) is scaled linearly with the pressure [28].

Table (1) Typical values of A and B constants, E/p and ionization energy (V_i) for various gases [2]

Gas	A (Ion/pairs)/(cm.torr)	B V/(cm.torr)	E/p V/(cm.torr)	V_i (V)
H_2	5	130	150~600	15.4
He	3	34 25	20~150 3~10	24.5
N_2	12	342	100~600	15.5
Ar	14	180	100~600	15.7
O_2	-	-	-	12.2
Ne	4	100	100~400	21.5
Kr	17	240	100~1000	14
Xe	26	350	200~800	12.1
Hg	20	370	200~600	10.4
Air	15	365	100~800	-
CO_2	20	466	500~1000	13.7
H_2O	13	290	150~1000	12.6

In case of small values of the product $p.d$, only few collisions occur and higher voltage is applied to increase the probability of breakdown per collision. Hence, the minimum voltage required to ignite the discharge of a gas sample of pressure p over a distance d is defined at the minimum of Paschen's curve, as [19]

$$pd|_{V_{min}} = \frac{1}{A} log\left(1 + \frac{1}{\gamma_e}\right) \quad (2)$$

If the pressure and/or inter-electrode distance is too large, ions generated in the gas are slowed by inelastic collisions, so that they strike the cathode with insufficient energy to produce secondary electrons. In most sputtering glow discharges, the discharge starting voltage is relatively high. Figure (4) shows the Paschen's curves of different gases. The electron mean free path (λ_e) is then related to the pressure by

$$\lambda_e \cong p.d \quad (3)$$

To initiate the discharge within the gas sample, the following condition must be satisfied [2]

$$p \geq \frac{\lambda_e}{d} \quad (4)$$

According to the self-sustaining feature of glow discharge, the number of the produced electrons is just sufficient to produce the same number of ions to generate again the same number of electrons. These ions liberate electrons from the electrodes (secondary), atom-ion and ion-ion collisions. When this condition is satisfied, the voltage decreases and the current increases. This is said to be a "normal discharge".

Due to the recombination effects and excited atoms returning to ground state, the plasma begins to glow, as

$$A^* \rightarrow A + hv \quad (4a)$$

$$A^+ + e^- \rightarrow A + hv \quad (4b)$$

here A^* is an excited atom and e^- is a high-energy electron

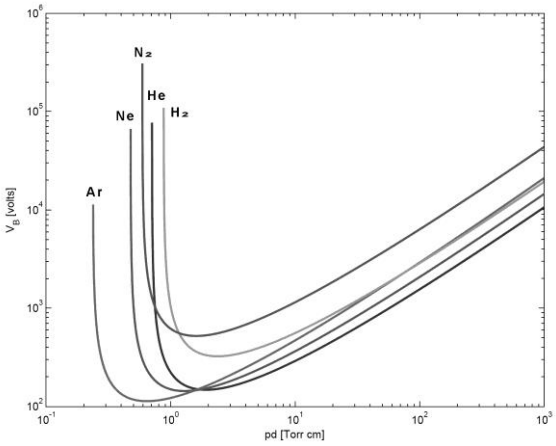

Fig. (4) Paschen's curves of different common gases used in electric discharge applications [21]

Table (2) shows the values of secondary electron emission coefficients for three different metals when different ions are bombarding these targets.

Table (2) The secondary electron emission coefficients for three different metals when different ions are bombarding these targets [2]

Target Material	Incident Ion	Ion Energy (eV)		
		200	600	1000
W	He^+	0.524	0.24	0.258
	Ne^+	0.258	0.25	0.25
	Ar^+	0.1	0.104	0.108
	Kr^+	0.05	0.054	0.108
	Xe^+	0.016	0.016	0.016
Mo	He^+	0.215	0.225	0.245
	He^{++}	0.715	0.77	0.78
Ni	He^+		0.6	0.84
	Ne^+			0.53
	Ar^+		0.09	0.156

3. Results and Discussion

Figure (5) shows the variation of secondary electron emission coefficient of cathode material with breakdown voltage of four different gases at pressure of 0.1 mtorr and inter-electrode distance of 4 cm. With such difference in the value of the emission coefficient (more than an order of magnitude), argon and nitrogen are highly preferred for using in discharge systems than hydrogen and helium. However, argon and nitrogen cannot replace helium in some applications of gas discharge, mainly gas lasers, as shown in Fig. (6). As well, hydrogen is the excellent choice for some other applications.

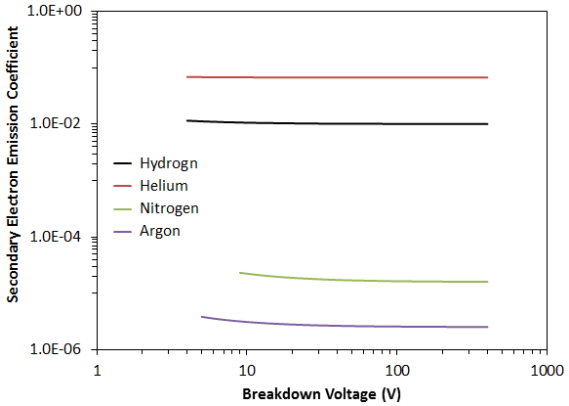

Fig. (5) Variation of secondary electron emission coefficient with breakdown voltage of four different gases at pressure of 0.1 mtorr and inter-electrode distance of 4 cm

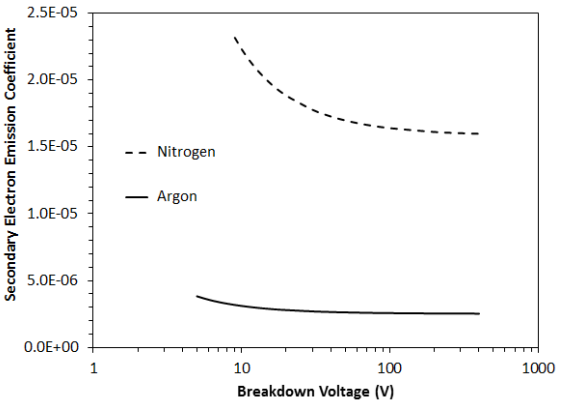

Fig. (6) Variation of secondary electron emission coefficient with breakdown voltage of four nitrogen and argon at pressure of 0.1 mtorr and inter-electrode distance of 4 cm

Figure (7) shows the variation of secondary electron emission coefficient of cathode material with gas pressure of four different gases at breakdown voltage of 200 V and inter-electrode distance of 4 cm. it is clear that all gases are similar at very low gas pressures. However, high gas pressures make small differences in the values of emission coefficient, which means that the secondary electron emission is unavoidable at high pressures and other parameters can be considered to minimize the emission coefficient.

Figure (8) shows the variation of secondary electron emission coefficient of cathode material with inter-electrode distance for four different gases at pressure of 0.2 mtorr and breakdown voltage of 200V. Working at small inter-electrode distances submit an advantage of low emission coefficient of secondary electrons. Though, most applications require gas discharges at inter-electrode distances larger than 2 cm as the values of the minimum emission coefficient ranging from 100 to 1000. Larger distances would reduce the emission coefficient by more than an order of magnitude but higher voltages will be required for gas breakdown.

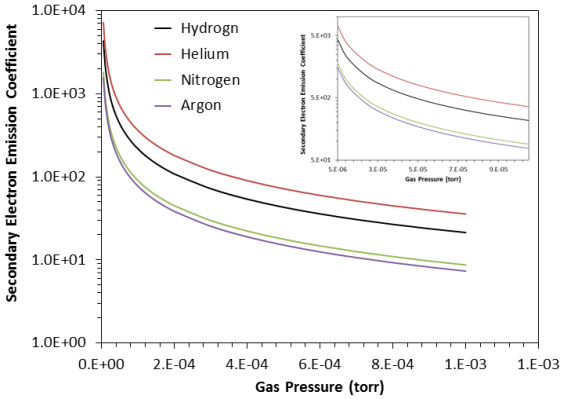

Fig. (7) Variation of secondary electron emission coefficient with gas pressure of four different gases at breakdown voltage of 200 V and inter-electrode distance of 4 cm

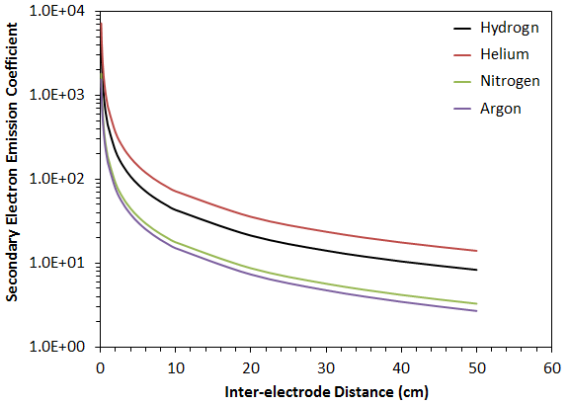

Fig. (8) Variation of secondary electron emission coefficient with inter-electrode distance for four different gases at pressure of 0.2 mtorr and breakdown voltage of 200 V

Helium is the most common gas in the practical uses of discharge plasmas, such as gas lasers and plasma processing. Therefore, it may be very advantageous to introduce the characteristics of secondary electron emission at experimental conditions (e.g., plasma sputtering). Figure (9) shows the variation of secondary electron emission coefficient of cathode material with gas pressure of helium at breakdown voltage of 190 V and inter-electrode distance of 4 cm. It is recommended to work at discharge gas pressures lower than 0.8 mtorr in order to keep the emission coefficient of secondary electrons lower than ten. Hence, the process employing discharge plasma can be performed with as much as possible investment of energy transferred to the discharge volume. This can be clearly observed in reactive sputtering processes as the electrical power remaining after the breakdown of discharge gas is mostly used for supporting the reaction of reactive gas with the sputtered atoms to form the required compound.

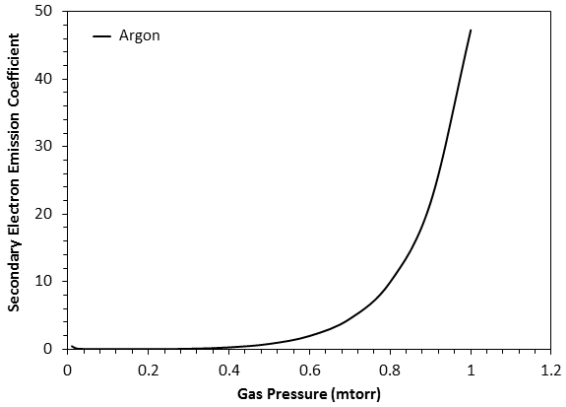

Fig. (9) Variation of secondary electron emission coefficient with gas pressure of helium at breakdown voltage of 190 V and inter-electrode distance of 4 cm

4. Conclusions

In concluding remarks, the emission coefficient of secondary electrons for some common gas discharges was determined as function of some affecting parameters. This coefficient has an important role in the optimization of discharge plasma employed for practical uses and applications. Therefore, this coefficient is often minimized even though the experimental conditions are shifted from their optima in order to ensure that the consumption of supplied power is high as much as possible. This study was supported by experimental data from a reactive plasma sputtering system.

References

[1] M. Ohring, **"The Materials Science of Thin Films"**, Academic Press, p. 79, 112 (1992).
[2] D. Huy Trinh, Nanocrystalline Alumina-Zirconia Thin Films Grown by Magnetron Sputtering, Linköping University, Sweden, (2008) p. 1.
[3] K. Wasa, M. Kitabatake, H. Adachi, **"Thin Film Materials Technology: Sputtering of Compound Materials"**, William Andrew Inc., p. 139, 116, 2, 119, 72, 106, 103, 9 (2004).
[4] O.A. Hammadi, M.K. Khalaf and F.J. Kadhim, "Fabrication of UV Photodetector from Nickel Oxide Nanoparticles Deposited on Silicon Substrate by Closed-Field Unbalanced Dual Magnetron Sputtering Techniques", *Opt. Quantum Electron.*, 47(12), 3805-3813 (2015).
[5] O.A. Hammadi, M.K. Khalaf, F.J. Kadhim, "Fabrication and Characterization of UV Photodetectors Based on Silicon Nitride Nanostructures Prepared by Magnetron Sputtering", *Proc. IMechE, Part N, J. Nanoeng. Nanosys.*, 230(1) 32-36 (2016).
[6] O.A. Hammadi, M.K. Khalaf and F.J. Kadhim, "Silicon Nitride Nanostructures Prepared by Reactive Sputtering Using Closed-Field Unbalanced Dual Magnetrons", *Proc. IMechE, Part L, J. Mater.: Design and Applications*, 231(5), 479-487 (2017).
[7] D.R. Gibson, "Deposition of multilayer optical coatings using closed field magnetron sputtering", online article (2006).
[8] B.T. Chiad et al., "Characteristics and Operation Conditions of a Closed-Field Unbalanced Dual Magnetrons Plasma Sputtering System", *Open Access Library J.* (OALib), 1 (2014) e650. DOI:10.4236/oalib.1100650
[9] O.A. Hammadi and N.E. Naji, "Characterization of Polycrystalline Nickel Cobaltite Nanostructures Prepared by DC Plasma Magnetron Co-Sputtering for Gas Sensing Applications", *Photon. Sens.*, 8(1), 43-47 (2018).
[10] O.A. Hammadi, F.J. Al-Maliki and E.A. Al-Oubidy, "Photocatalytic Activity of Nitrogen-Doped Titanium Dioxide Nanostructures Synthesized by DC Reactive Magnetron Sputtering Technique", *Nonl. Opt. Quant. Opt.*, 51(1/2), 67-78 (2019)
[11] O.A. Hammadi et al., "Key Mechanisms of Low-Pressure Glow Discharge in Magnetized Plasmas", *Iraqi J. Appl. Phys.*, 12(3) (2016) 3-12.
[12] O.A. Hammadi et al., "Employment of Magnetron to Enhance Langmuir Probe Characteristics of Argon Glow Discharge Plasma in Sputtering System", *Iraqi J. Appl. Phys.*, 12(4) (2016) 19-28.
[13] M.A. Lieberman and A.J. Lichtenberg, **"Principles of Plasma Physics and Materials Processing"**, 2nd ed., Wiley (2005), p. 535, 547.
[14] M.K. Khalaf, O.A. Hammadi and F.J. Kadhim, "Current-Voltage Characteristics of DC Plasma Discharges Employed in Sputtering Techniques", *Iraqi J. Appl. Phys.*, 12(3) (2016) 11-16.
[15] O.A. Hammadi et al., "Operation Characteristics of a Closed-Field Unbalanced Dual-Magnetrons Plasma Sputtering System", *Bulg. J. Phys.*, 41 (2014) 24-33.
[16] F.F. Chen, **"Introduction to Plasma Physics and Controlled Fusion"**, 2nd ed., Plenum Press (NY, 1974), p. 22.
[17] C. O'Leary, Design, Construction and Characterisation of a Variable Balance Magnetron Sputtering System, Dublin City University, Ireland, p. 15 (1999).
[18] R.A. Swady, Development of vacuum technologies for the preparation of high-purity thin films in simple systems, PhD thesis, Loughborough University of Technology (1992), pp. 4-7, 19-21.
[19] T.J. Boyd and J. Sanderson, **"Physics of Plasmas"**, Cambridge University Press (2003).
[20] H.B. Nie, Thin Film Deposition and Characterization, National University of Singapore (NUS) (2014).
[21] B. Shah, Deposition of Tantalum on Steel by Sputtering, MSc thesis, New Jersey Institute of Technology (2001), p. 3, 15, 30.
[22] M. Julfikar Haider, Deposition of Hard and Solid Lubricant (TiN+MoS_x) Coating by Closed-Field Magnetron Sputtering, PhD thesis, Dublin University, Ireland (2005), pp. 56-58, 176.

[23] B.T. Chiad et al., "Langmuir Probe Diagnostics of Low-Pressure Glow Discharge Plasma Using Argon-Nitrogen Mixtures", *Iraqi J. Appl. Phys.*, 12(3) (2016) 17-26.
[24] O.A. Hammadi et al., "Magnetic Field Distribution of Closed-Field Unbalanced Dual Magnetrons Employed in Plasma Sputtering Systems", *Iraqi J. Appl. Phys.*, 12(3) (2016) 34-42.
[25] T. Tavsanoglu, Deposition and characterization of single and multilayered BC and BCN thin films by different sputtering configurations, PhD thesis, Université Technique d'Istanbul, Ecole des Mines de Paris (2009), p. 2, 16-23, 29.
[26] M.B. Hendricks et al., "Effects of ion-induced electron emission on magnetron plasma instabilities", *J. Vac. Sci. Technol.*, A12(4) (1994) 1408-1416.
[27] P.M. Martin, **"Introduction to Surface Engineering and Functionally Engineered Materials"**, John Wiley & Sons, Inc. (2011), p. 339.
[28] F. Ghaleb and A. Belasri, "Numerical and theoretical calculation of breakdown voltage in the electrical discharge", Radiation Effects and Defects in Solids, 1 (2012) 1-7.

IRAQI JOURNAL OF APPLIED PHYSICS
Vol. 16, No. 1, January-March 2020, 21-24

Effect of Annealing Temperature on Urbach Energy for $CdO:In_2O_3$ Thin Films Prepared by Pulsed-Laser Deposition

Amer A. Ramadhan

Department of Physics, College of Science, University of Baghdad, Baghdad, IRAQ

In this work, $CdO:In_2O_3$ thin films with 50:50 molar ratio were prepared by pulsed-laser deposition technique and annealed at different temperatures (373, 473 and 573 K) to study the effect of annealing on their structural, morphological and optical properties. The x-ray diffraction measurements showed that these thin films are polycrystalline and their crystallinity was enhanced with increasing annealing temperature. The UV-visible spectral measurements showed that Urbach energy was decreased with increasing annealing temperature, which causes to reduce the optical band gap energy of the prepared samples. These thin films were successfully employed for gas sensing applications.

Keywords: Urbach energy; $CdO:In_2O_3$; Thermal annealing; Pulsed-laser deposition
Received: 4 January 2020; **Revised:** 12 February 2020; **Accepted:** 19 February 2020

1. Introduction

Transparent conductivity oxides (TCOs) are continuously introduced in many photonic and optoelectronic applications. One of the most important materials in this field is indium oxide (In_2O_3) with good specifications as it is a wide band-gap semiconductor with cubic crystalline structure. Due to its high optical transparency and high electrical conductivity, it is intensively used in solar cells, flat panel displays (FPDs) [1,2]. The pursuit of high-quality transparent thin films has made many research works looking for alternative materials, using new methods or changing deposition parameters.

Cadmium oxide (CdO) is an n-type semiconductor with a simple cubic structure and direct optical band gap of 2.3 eV [3]. Among the transparent conductive oxide (TCOs), the excellent properties of CdO make it an important candidate for important studies [4]. CdO thin films have extraordinary properties those qualify it to use in various optoelectronic industries [5].

Bulk-heterojunction can be fabricated by well-mixed of two components in one layer. Compared to the bilayer design, the bulk-heterojunction provides a larger interfacial area which is beneficial for the formation of the charge-transfer state [6]. The impurities, irregularities, or differences in average grain size in semiconductors cause the static disorder of the lattice in addition to dynamic disorder induced by phonons. Both disorders contribute to the tail states near the bands edges [7].

Pulsed-laser deposition (PLD) technique is a simple method used to deposit metal, semiconducting, insulating and organic materials such as polymers, as single or mixture of different materials. In PLD, short laser pulses with high energy are used to evaporate or sublimate material from the target to deposit on substrate opposite to target surface [5].

Annealing is one of the common ways to improve the structural, optical and electrical properties of thin films after preparation [8].

2. Experimental Work

Cadmium oxide powder (CdO) with 99.9% purity and indium oxide (In_2O_3) with 99.9% purity supplied by American Elements were mixed with 50:50 ratio. The $CdO:In_2O_3$ target, with 1 cm diameter, was fabricated using hydraulic piston under 3 ton press in stainless steel mold. Thin films were prepared by pulsed-laser deposition technique inside a glass chamber evacuated down to 10^{-2} mbar by a rotary pump. The prepared films were annealed in closed furnace, with oxygen flow, at different temperatures (373, 473 and 573 K) for 30 min. Finally, the samples were examined by x-ray diffraction (XRD), atomic force microscopy (AFM) and UV-visible spectroscopy to study the effect of annealing temperature on structural, morphological and optical properties of the prepared films.

3. Results and Discussions

Figure (1) shows the XRD patterns for prepared composite $CdO:In_2O_3$ thin films deposited on glass substrate and annealed at different temperatures. The amorphous structure of the as-deposited samples has converted to polycrystalline structure after thermal annealing. The crystallinity was enhanced, as the peak intensities have increased, with increasing annealing temperature due to removing the disorder within the lattice. The peaks appeared in Fig. (1) are

corresponding to both lattice planes of the two initial phases of In_2O_3 (according to JCPDS card No. 96-101-0589) and for CdO (according to JCPDS card No. 96-900-6690), i.e., no new phase was observed, which indicates the formation of mixed samples.

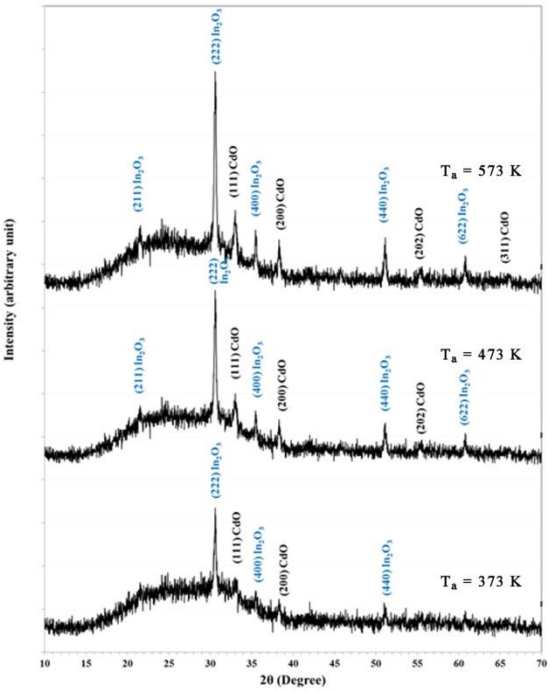

Fig. (1) XRD patterns for CdO:In_2O_3 thin films annealed at different temperatures

The peak broadening was measured by Lorentzian fitting and the crystallite size was calculated using Debye-Scherrer's formula [9]. Figure (2) shows the fitting of preferred peak along (222) miller indices using X-Powder Software and Table (1) illustrates the XRD peaks and the comparison between calculated inter-planar distance, standard and experimentally determined crystallite size. It seems that the average crystallite size increases with increasing annealing temperature.

Figure (3) illustrates the 3D AFM images for the prepared composite CdO:In_2O_3 thin films and annealed at different temperatures as well as the percentage distribution of particle size. The as-deposited film at 373 K appeared to include nanoparticles with spherical shape and they converted into rod shape after annealing at 473 and 573 K. The rod diameters were measured using ImageJ program as illustrated in Fig. (4), which has small increment by annealing from about 100 nm to 130 nm diameter for the selected point of filament shape.

Table (2) illustrates the parameters of surface morphology (average diameter and root mean square roughness) for CdO:In_2O_3 thin films annealed at different temperatures. The average diameter of particle aggregations increases with increasing annealing temperature due to the incorporation between adjacent particles.

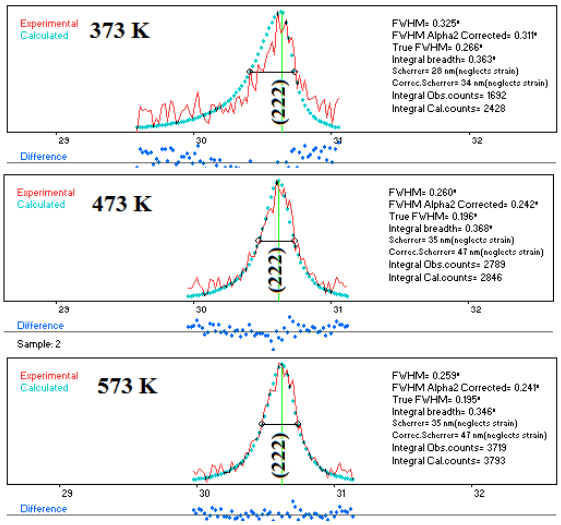

Fig. (2) Lorentzian fitting for the preferred orientation peak along (222) direction

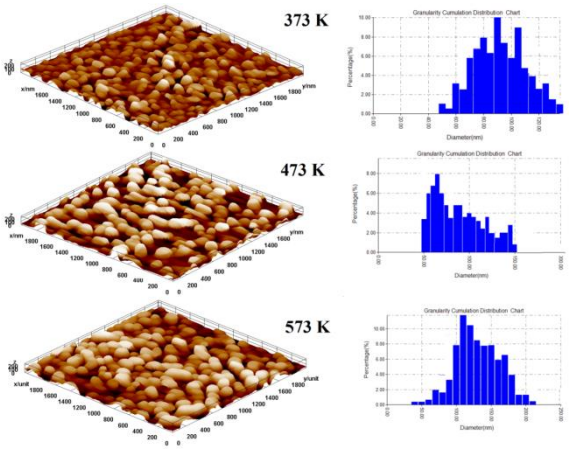

Fig. (3) 3D AFM image and the granularity distribution for CdO:In_2O_3 thin films annealed at different temperatures

Figure (5) shows the transmission spectra of the composite CdO: In_2O_3 thin films annealed at different temperatures. In general, as in all semiconductors, the transmittance increases with incident wavelength and is almost constantly high at longer wavelengths as the low photon energy is not enough to interact with electrons in valence band. The transmittance increases to more than 90% as the annealing temperature is increased to 573 K. Also, the absorption edge is seen to be much sharper when the annealing temperature is increased, where the exponential region is limited within a short wavelength range, indicating a decrease in local states near the absorption edge due to the decrease of crystalline defects.

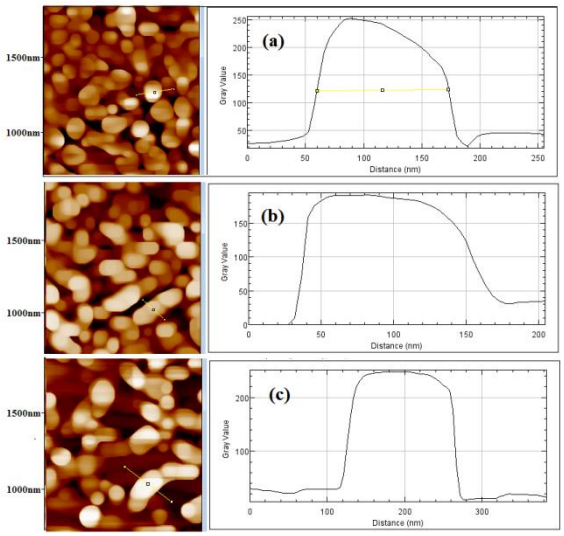

Fig. (4) Calculation of rod diameter in the three samples annealed at different temperatures (a) 373 K (b) 473 K and (c) 573 K

Table (2) Average diameter and RMS roughness for $CdO:In_2O_3$ thin films annealed at different temperatures

T_a (K)	Average Diameter (nm)	RMS roughness (nm)
373	95.73	2.85
473	100.85	2.31
573	123.11	1.79

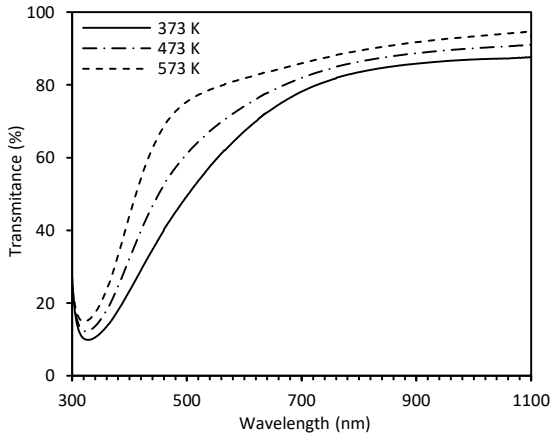

Fig. (5) UV-visible transmission $CdO:In_2O_3$ thin films annealed at different temperatures

The energy band gap was determined by extrapolation of the straight segment of the curve between $(\alpha h\upsilon)^2$ and photon energy ($h\upsilon$) according to Tauc formula. Note that the optical energy band gap (E_g) is increased from 2.9 to 3.1 eV as the annealing temperature was increased from 373 to 573 K. The reason of slight increase in the energy band gap with increasing annealing temperature may be attributed to the reduction of Urbach energy with crystallization improvement. This result agrees with results of Ali et al. [10]. The main reason for studying the Urbach parameters is to find disordering processes in solids. The exponential increase of the absorption around the absorption edge is explained by transitions between the tails of density-of-states in the valence and conduction bands. The tail width depends on the presence of different types of defects [11]. The Urbach energy is equal to the width of absorption edge, which is reciprocal to the slope of linear part of the relation between $\ln(\alpha)$ and photon energy ($h\upsilon$) at the absorption edge [12]. From Fig. (7), it seems that the line slope increases with increasing annealing temperature, which indicates the decrease of tail width, as shown in Table (3).

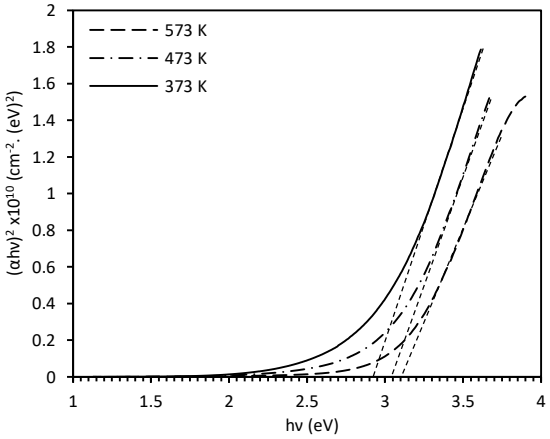

Fig. (6) Tauc formula for $CdO:In_2O_3$ thin films annealed at different temperatures

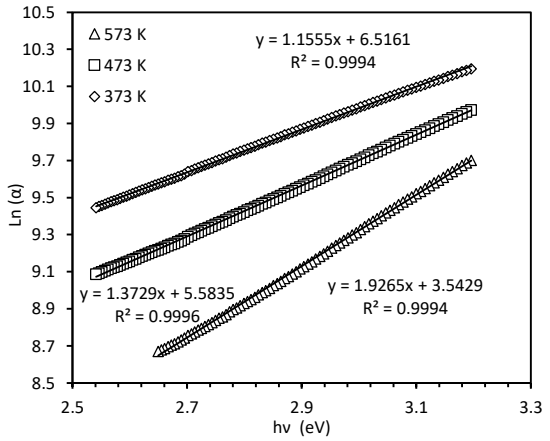

Fig. (7) Determination of Urbach energy for $CdO:In_2O_3$ thin films annealed at different temperatures

Table (3) Optical band gap and Urbach energy for $CdO:In_2O_3$ thin films annealed at different temperatures

T_a (K)	E_g (eV)	λ_c (nm)	Urbach energy (eV) (1/slope)
373	2.90	428	0.87
473	3.00	413	0.73
573	3.10	400	0.52

Conclusions

Composite CdO:In_2O_3 thin films were prepared by pulsed-laser deposition technique and the effect of thermal annealing on their properties were studied. The crystallinity of this composite was enhanced and their crystallite size was increased with increasing annealing temperature. Thermal annealing resulted in a variation in the shape of nanostructures from spherical to rods. The Urbach energy of the prepared composite was decreased with increasing annealing temperature, which expresses the disorder degree of the prepared solid state samples.

References

[1] S. Kaleemulla et al., "Effect of Annealing on Structural and Optical Properties of Cu Doped In_2O_3 Thin Films," *J. NANO- Electron. Phys.*, 5(4) (2013) 1–4.

[2] X.Y. Kong and Z.L. Wang, "Structures of indium oxide nanobelts," *Solid State Commun.*, 128(1) (2003) 1–4.

[3] B. Gokul, P. Matheswaran, and R. Sathyamoorthy, "Influence of Annealing on Physical Properties of CdO Thin Films Prepared by SILAR Method," *J. Mater. Sci. Technol.*, 29(1) (2013) 17–21.

[4] A.O. Alkhayatt, I.A.D. Al-hussainy and O.A.C. Al-rikaby, "Annealing Effect on the Structural and Optical Properties of Sol-Gel Deposited Nanocrystalline CdO Thin Films," *Adv. Phys. Theor. Appl.*, 34 (2014) 2225–638.

[5] K. Siraj et al., "Effect of deposition temperature on structural, surface, optical and magnetic properties of pulsed laser deposited Al-doped CdO thin films," *J. Alloys Compd.*, 509(24) (2011) 6756–6762.

[6] C. Lindqvist, *Stability of Bulk-Heterojunction Blends for Solar Cell Applications*. 2014.

[7] V.P. Kunets et al., "Urbachs rule peculiarities in structures with CdS_xSe_{1-x} nanocrystals," *Semicond. Physics, Quantum Electron. Optoelectron.*, 5(2) (2002) 9–15.

[8] M.A. Flores-mendoza et al., "Influence of the annealing temperature on the properties of undoped indium oxide thin fi lms obtained by the sol-gel method," *Thin Solid Films*, 517(2) (2008) 681–685.

[9] P. Scherrer, "Göttinger Nachrichten Gesell", 2 (1918) 98.

[10] H.M. Ali et al., "Properties of transparent conducting oxides formed from CdO alloyed with In_2O_3", *Thin Solid Films*, 515 (2007) 3024–3029.

[11] G.D. Cody, "Urbach edge of crystalline and amorphous silicon: a personal review", *J. Non-Cryst. Solids*, 141 (1992) 3-15.

[12] I. Studenyak, M. Kranj and M. Kurik, "Urbach Rule in Solid State Physics," *Int. J. Opt. Appl.*, 4(3) (2014) 76–83.

Table (1) XRD parameters for CdO:In_2O_3 thin films prepared in this work and annealed at different temperatures

T_a (K)	2θ (deg.)	FWHM (deg.)	d_{hkl} Exp. (Å)	G.S. (nm)	(hkl)	d_{hkl} Std. (Å)	Phase
373	30.5882	0.3250	2.9203	20.24	(222)	2.9214	Cub. In_2O_3
	33.1222	0.6334	2.7024	13.09	(111)	2.6848	Cub. CdO
	35.4299	0.4525	2.5315	18.44	(400)	2.5300	Cub. In_2O_3
	38.3258	0.4525	2.3467	18.59	(200)	2.3251	Cub. CdO
	50.9955	0.4072	1.7894	21.62	(440)	1.7890	Cub. In_2O_3
473	21.5385	0.4072	4.1225	19.87	(211)	4.1315	Cub. In_2O_3
	30.5882	0.2600	2.9203	30.35	(222)	2.9214	Cub. In_2O_3
	33.0317	0.4071	2.7096	20.36	(111)	2.6848	Cub. CdO
	35.4751	0.3168	2.5284	26.34	(400)	2.5300	Cub. In_2O_3
	38.3258	0.3620	2.3467	23.24	(200)	2.3251	Cub. CdO
	51.1312	0.3620	1.7850	24.34	(440)	1.7890	Cub. In_2O_3
	55.4751	0.4072	1.6551	22.05	(202)	1.6441	Cub. CdO
	60.8145	0.4977	1.5219	18.51	(622)	1.5256	Cub. In_2O_3
573	21.5338	0.4019	4.1234	20.13	(211)	4.1315	Cub. In_2O_3
	30.6162	0.2590	2.9177	31.57	(222)	2.9214	Cub. In_2O_3
	33.0275	0.4018	2.7100	20.63	(111)	2.6848	Cub. CdO
	35.5191	0.3215	2.5254	25.96	(400)	2.5300	Cub. In_2O_3
	38.3322	0.2813	2.3463	29.91	(200)	2.3251	Cub. CdO
	51.1520	0.3616	1.7843	24.37	(440)	1.7890	Cub. In_2O_3
	55.3717	0.4420	1.6579	20.31	(202)	1.6441	Cub. CdO
	60.7971	0.3616	1.5223	25.48	(622)	1.5256	Cub. In_2O_3
	66.0616	0.4420	1.4132	21.45	(311)	1.4021	Cub. CdO

THE IRAQI JOURNAL OF APPLIED PHYSICS
EDITORIAL BOARD

COPYRIGHT RELEASE FORM
IRAQI JOURNAL OF APPLIED PHYSICS (IJAP)

We, the undersigned, the author/authors of the article titled

……
……
……
……
……
……
……

that is submitted to the Iraqi Journal of Applied Physics (IJAP) for publication, declare that we have neither taken part or full text from any published work by others, nor presented or published it elsewhere in any other journal. We also declare transferring copyrights and conduct of this article to the Iraqi Journal of Applied Physics (IJAP) after accepting it for publication.

The authors will keep the following rights:

1. Possession of the article such as patent rights.
2. Free of charge use of the article or part of it in any future work by the authors such as books and lecture notes after informing IJAP editorial board.
3. Republishing the article for any personal purposes of the authors after taking journal permission.

To be signed by all authors:

Signature:……..date: ……
Printed name: ……

Signature:……..date: ……
Printed name: ……

Signature:……..date: ……
Printed name: ……

Correspondence
address:……..……...
……
Address:……..……
……
Telephone:……..……..email: ……

Note: Complete and sign this form and mail it to the below address with your finally revised manuscript

The Iraqi Journal of Applied Physics
www.iraqiphysicsjournal.com
Email: info@iraqiphysicsjournal.com
Email: editor_ijap@yahoo.co.uk
Email: irq_appl_phys@yahoo.com

IRAQI JOURNAL OF APPLIED PHYSICS

Volume (16), Issue (1), January-March 2020

CONTENTS